JOURNAL OF QUATERNARY SCIENCE (2023) **38**(6) 891–920 ISSN 0267-8179. DOI: 10.1002/jqs.3527

JQS Journal of Quaternary Science QRA Quaternary Research Association

Chronological constraint of Neanderthal cultural and environmental changes in southwestern Europe: MIS 5–MIS 3 dating of the Axlor site (Biscay, Spain)

MARTINA DEMURO,[1] LEE J. ARNOLD,[1] JESÚS GONZÁLEZ-URQUIJO,[2]* TALIA LAZUEN[2,3] and MANUEL FROCHOSO[2]

[1]School of Physical Sciences, Environment Institute, and Institute for Photonics and Advanced Sensing (IPAS), University of Adelaide, Adelaide, SA, Australia

[2]Instituto Internacional de Investigaciones Prehistóricas de Cantabria, IIIPC-University of Cantabria, Edificio Interfacultativo, Universidad de Cantabria, Santander, Spain

[3]CNRS, MCC, PACEA, UMR 5199, Univ. Bordeaux, Pessac, France

Received 25 October 2022; Revised 4 April 2023; Accepted 12 April 2023

ABSTRACT: The cave site of Axlor (Biscay, Spain) preserves one of the most informative Middle Palaeolithic (MP) records for the North Atlantic Iberian region, though its age remains poorly known. Here we use single-grain optically stimulated luminescence (OSL) and single-grain thermally transferred OSL (TT-OSL) dating of sediments to improve the age constraint of Axlor's MP succession (levels N–B). Our new ages are consistent with the previously published *terminus ante quem* ^{14}C ages for the site (>42.9 cal ka BP), and suggest the sequence accumulated during a period of ~50 kyr. Axlor's levels N–F were deposited ~100–80 ka, probably during marine isotope stage (MIS) 5d–a, while levels D and B were deposited ~70 and ~50 ka, respectively, during MIS 4 and mid-MIS 3. Our results indicate that major faunal and technological turnovers occurred towards the end of MIS 5, potentially coinciding with broader environmental and climatic changes. Axlor's Quina record, dated here to the onset of MIS 4, is one of the oldest in Europe. Comparisons with neighbouring sites point to complex regional chronologies and development for this particular behaviour, though detailed correlations with other MP sequences remain difficult due to their poor chronological attributes. The present study highlights the important role that single-grain optical dating can play in elucidating the broader evolution of the MP across southwestern Europe.

KEYWORDS: Axlor; Late Pleistocene; Middle Palaeolithic; Neanderthal; Quina; single-grain OSL; single-grain TT-OSL

Introduction

The Middle Palaeolithic record of the North Atlantic Iberian region, which encompasses parts of Galicia, Asturias, Cantabria, Basque Country and Navarre provinces of Spain (Figure 1), is of major significance for understanding the evolutionary and extinction dynamics of Neanderthal populations – discussions that started with the pioneering work of H. Obermaier in the cave of El Castillo (Obermaier, 1916) (Cantabria province). The archaeological information available from this region is central to several ongoing scientific debates regarding Neanderthal behaviour, including: the oldest possible symbolic-graphic expressions in parietal support (in La Pasiega; Hoffmann et al., 2018), early use of standardized hunting weapons (Lazuén, 2012), the existence of bedding areas in caves (Cabanes et al., 2010) and types of social relations uncovered by palaeogenetic analysis (Lalueza-Fox et al., 2011). Additionally, the region plays a key role in understanding the Middle-to-Upper Palaeolithic transition and investigating the process of Neanderthal extinction, with sites such as Cueva Morín, Ekain and Le Basté recording some of the latest occupations of these populations at the end of the Mousterian and during the Chatelperronian (Bachellerie, 2011; Gonzalez Echegaray, 1971).

In general, the chronological framework of Middle Palaeolithic records from the North Atlantic Iberian region is poorly constrained due to a lack of well-dated stratigraphic sequences. Radiocarbon (^{14}C) dating is the most widely used geochronology approach, though many Middle Palaeolithic sites lie well beyond the ^{14}C calibration age range (~55 cal ka BP; Reimer et al., 2020) and thus remain essentially undated owing to the limited uptake of alternative radiometric techniques. Historically, there has also been a reliance on ^{14}C chronologies obtained with suboptimal analytical techniques that may not completely remove organic contaminants, which has resulted in inferior quality late Neanderthal chronological schemes at some sites. While the advent of more rigorous ^{14}C extraction procedures [e.g. ultrafiltration, acid base oxidation-stepped combustion (ABOx-SC)] has improved terminal Neanderthal chronologies for parts of the region (e.g. Higham et al., 2014; Wood et al., 2018; Wood et al., 2013a), their widespread application can be hindered by poor organic preservation (e.g. Wood et al., 2013b). The potential therefore remains for seemingly finite ages to be obtained at some Middle Palaeolithic sites lying at, or beyond, the upper ^{14}C dating limit if minor contaminants cannot be fully eliminated by available methodologies (e.g. Demuro et al., 2019a; Hublin, 2017; Zilhão et al., 2020; Zilhão et al., 2021a). These chronological shortcomings have made it

*Correspondence: Jesús González-Urquijo, as above.
Email: jesuse.gonzalez@unican.es

difficult to reliably examine the longer term occupation dynamics of Neanderthal groups in the region, and to ascertain potential palaeoenvironmental drivers of behavioural and cultural adaptations (Deschamps, 2017; Lazuen, 2012). There thus remains a need to re-evaluate the Middle Palaeolithic history of North Atlantic Iberia using a broader suite of dating methods. Single-grain optically stimulated luminescence (OSL) dating of sedimentary quartz (e.g. Murray et al., 2021) offers a potentially useful means of cross-checking and breaking through the '^{14}C barrier', and this technique has recently been used to establish reliable chronologies at a range of Iberian Middle Palaeolithic sites (e.g. Arnold et al., 2013; Arnold et al., 2016; Benito-Calvo et al., 2020; Daura et al., 2021; Demuro et al., 2019a; Ruiz et al., 2021; Zilhão, 2021; Zilhão et al., 2020; Zilhão et al., 2021a).

The site of Axlor is a key locality for understanding the Middle Palaeolithic history of North Atlantic Iberia. The site is significant because it preserves one of the most informative Middle Palaeolithic sequences of the region; it contains a succession of 11 well-defined and intact stratigraphic levels (González-Urquijo, et al., 2006; González-Urquijo, et al., 2014; Lazuen and González-Urquijo, 2020) with Neanderthal remains (particularly dental) in practically all levels, abundant archaeological assemblages, several well-preserved combustion structures and the presence of bone industry, among other finds. The stratigraphic and archaeological record reflects elements of continuity, but the site also preserves evidence of important cultural changes in the upper units. These changes can be seen in the type of fauna hunted (predominance of deer remains is replaced by *Bison*/*Equus*) and approaches to stone tool management (from raw materials to knapping techniques – i.e. Levallois in the lower levels is overlain by typical Quina assemblages), as well as in the economic strategies and mobility systems represented in the archaeological succession (see Supporting Information).

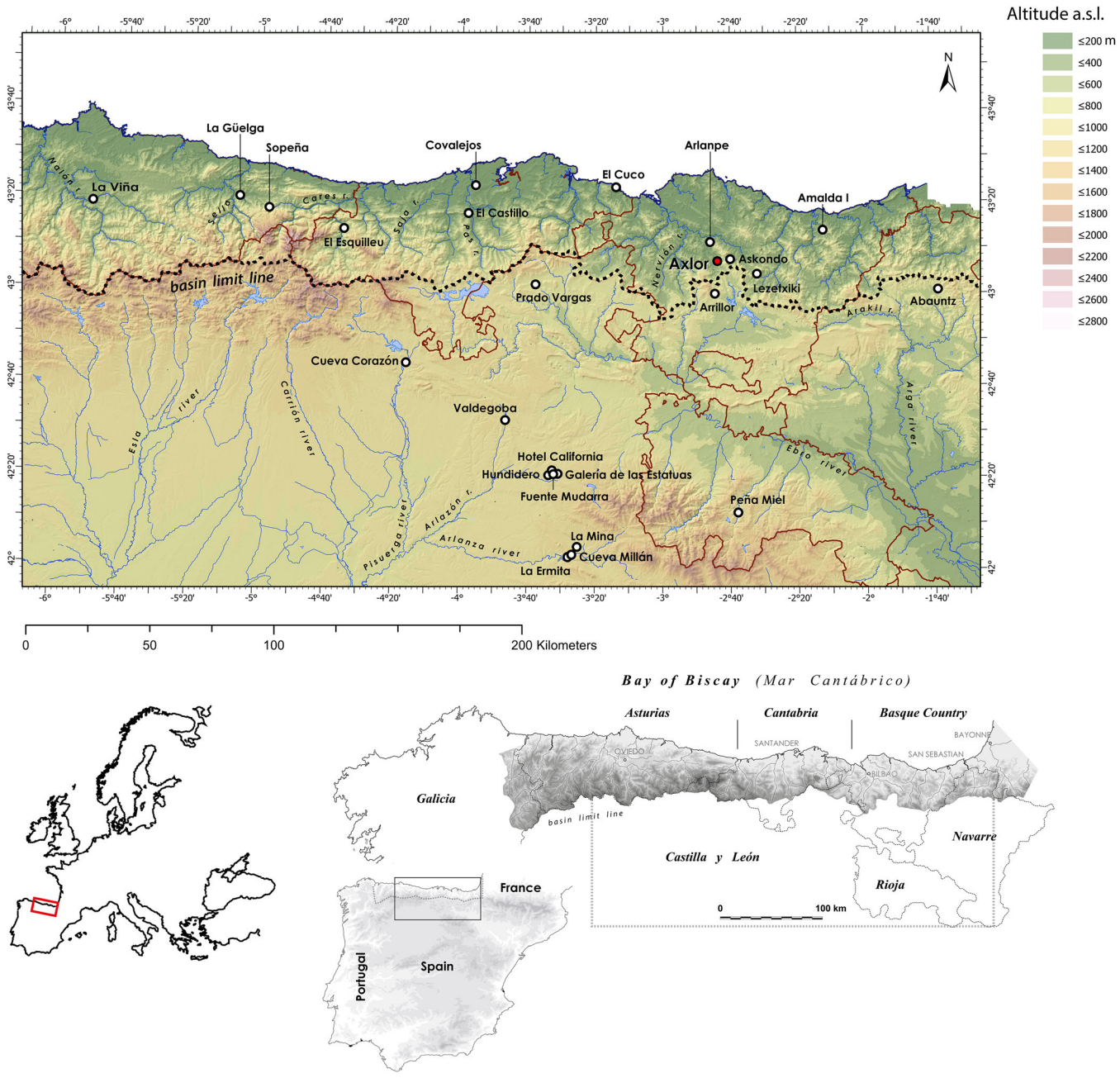

Figure 1. Location of Axlor (Dima, Biscay) in the North Atlantic Iberian region, which is highlighted in the middle map and demarcated by the dashed line in the top map. Also shown are other sites mentioned in the text and listed in Table 6 that are located in the North Atlantic Iberian region and the adjacent regions to the south. [Color figure can be viewed at wileyonlinelibrary.com]

Axlor was first excavated between 1967 and 1974 (Barandiarán, 1980). In these initial studies, J. M. de Barandiarán defined nine archaeological levels, six of them Mousterian (levels III–VIII) and three located at the top (levels I, II) and base (level IX) of the sequence, which were deemed sterile. A new excavation and research programmem began at Axlor in 2000, which included the acquisition of the first numerical dating results for the site (González-Urquijo, et al., 2005). A new stratigraphic framework was also defined (see 'Stratigraphy' below for details), which was reinterpreted as being composed of 11 archaeological levels (levels A–S), with only one of them being sterile (level P). The initial numerical ages obtained for Axlor during the recent excavations were based on ^{14}C dating of bone (outlined in the Supporting Information; Table S1). These results suggested that the upper part of the Middle Palaeolithic sequence (levels F–B) ranged between ~42 and >47.5 (uncalibrated) ^{14}C ka BP, with several samples yielding infinite and stratigraphically inverted calibrated age ranges indicative of potential contamination issues (González-Urquijo, et al., 2005; González-Urquijo et al., 2021). As it appeared that the archaeological sequence extended beyond the upper age limit of ^{14}C dating (~50 ka), the technique was not applied to the underlying levels (S–M). The oldest part of the Axlor sequence therefore remains undated and its temporal relationship with other sites has not yet been established.

To confirm the poor suitability of the ^{14}C chronology for the site, and to determine the timing of the occupations represented in the lower levels, we have initiated a comprehensive OSL dating study of the Axlor sedimentary sequence as part of the recent excavations. In this paper we present the results of the new optical dating programme, which aims to (i) establish a more robust chronological framework for key cultural changes recorded in the Axlor archaeological sequence and (ii) provide improved insights into the evolution and palaeoenvironmental context of the regional Middle Palaeolithic succession. The single-grain OSL analyses presented herein focus on the sedimentary sequence spanning levels N–B of Axlor. This sedimentary package contains several stratigraphic units with Mousterian occupations, as well as distinctive palaeoenvironmental indicators inferred from faunal assemblages. We additionally apply a semi-independent, extended-range optical dating technique (single-grain thermally transferred OSL; TT-OSL; e.g. Arnold et al., 2015) to the lowermost dated level (level N) to cross-check the suitability of the OSL dating results. After detailing our chronological findings, we go on to discuss the implications of the new dating results in terms of site accumulation history, the timing and significance of cultural changes preserved in the archaeological succession, potential palaeoenvironmental inferences, and correlations with other Middle Palaeolithic records across the region.

Study site

Location

The site of Axlor (43°07.3′N, 02°43.7′W; 315 masl) is located in the municipality of Dima (Basque country, Spain) within the Indusi karst – a small karst system formed in the Supraurgonian limestone of the upper Arratia valley (Figure 2). The local environment is mountainous and rocky, though the site is situated in a coastal region, currently ~30 km from the coastline. The valley where the site is located constitutes one of the lowest points connecting the Atlantic and Mediterranean regions of the Iberian Peninsula (Figure 3), and marks the biogeographical border between the Eurosiberian and Mediterranean regions (Moreno et al., 1990).

Axlor cave is located in the upper section of a series of at least three overlapping galleries, the lowest of which currently functions as a discharge point for the Indusi karst. The cave is about 20 m above the current level of water circulation. Sedimentary deposits have almost completely filled the mouth of the cave during the Late Pleistocene.

Stratigraphy

The stratigraphic sequence comprises 11 levels: A–P (Figure 4) and levels R and S. Levels A-1 and A-2 are practically sterile, with some isolated spots containing small amounts of material attributable to the Upper Palaeolithic. Level A-1 is matrix-supported, and massive, with no apparent structure. The sediment from this level is composed of silty clay with limestone clasts of variable size (ranging from metre to centimetre scale), and the layer accumulated for up to 110 cm before reaching the ceiling of the cave. Level A-2 thickens towards the eastern wall, where it acquires the greatest thickness (several tens of centimetres). It represents a formation of brown fine elements dominated by silts and clays (>80%). It preserves an alternating sequence of thin beds (1 or 2 cm) made up of fine gravel, which are wedged towards the north, and thicker (up to 10 cm) clay-loam layers. This arrangement produces a banded structure and is probably the result of continuous, non-turbulent (almost laminar) water flow, which facilitated decantation of the fines, alternating with periods of increased energy currents. There is no evidence of anthropic occupation in this deposit (González-Urquijo, et al., 2006; González-Urquijo, 2009).

The Middle Palaeolithic sequence at Axlor extends from level N at the base to B at the top. This part of the sequence is the subject of the present study. Here, most of the sedimentary infill represents anthropic materials, waterlain facies and entrance facies (as defined by Karkanas and Goldberg, 2019), which include incorporation of colluvial material from the slopes surrounding the cave opening. Details of the stratigraphic sequence have been provided previously in González-Urquijo et al. (2006), González-Urquijo et al. (2014) and Lazuen and González-Urquijo (2020), and can be summarized as follows (see Tables S2 and S3, and Figs. S2–S5).

Level B is a 5- to 10-cm-thick detrital bed of yellowish tones, composed of fine elements that include sporadic, widely scattered gravel and limestone pebbles. The abundant matrix is mainly made up of clays and silts (>80%). Sands are more scarce and show a bias towards the fine sand size fraction (>70% of the total sand fraction), with the mode and median being 0.125–0.080 and 0.08–0.065 mm, respectively (Fig. S4). The clastic materials from Level B show limited evidence for displacement, as reflected by a predominance of angular elements and minimal wear, except for some sporadic sub-rounded or rounded elements. The lithic industry is dominated by scrapers and the main raw materials are flint and quartz (~50 and ~30%, respectively). Most of the flint tools are made from flakes produced outside the site, with knapping systems that are difficult to ascertain due to the extreme degree of use/resharpening of the supports. The local rocks – quartz and lutite – have often been worked *in situ*. In the case of lutite, unipolar schemes were followed to generate larger and more elongated flakes (González Urquijo et al., 2005; 2006; 2014). The density of >4-mm-long lithic remains in level B range between 5400 and 10,100 m^{-3}, and the faunal composition is predominantly *Bison*, *Cervus* and *Equus* (>60%).

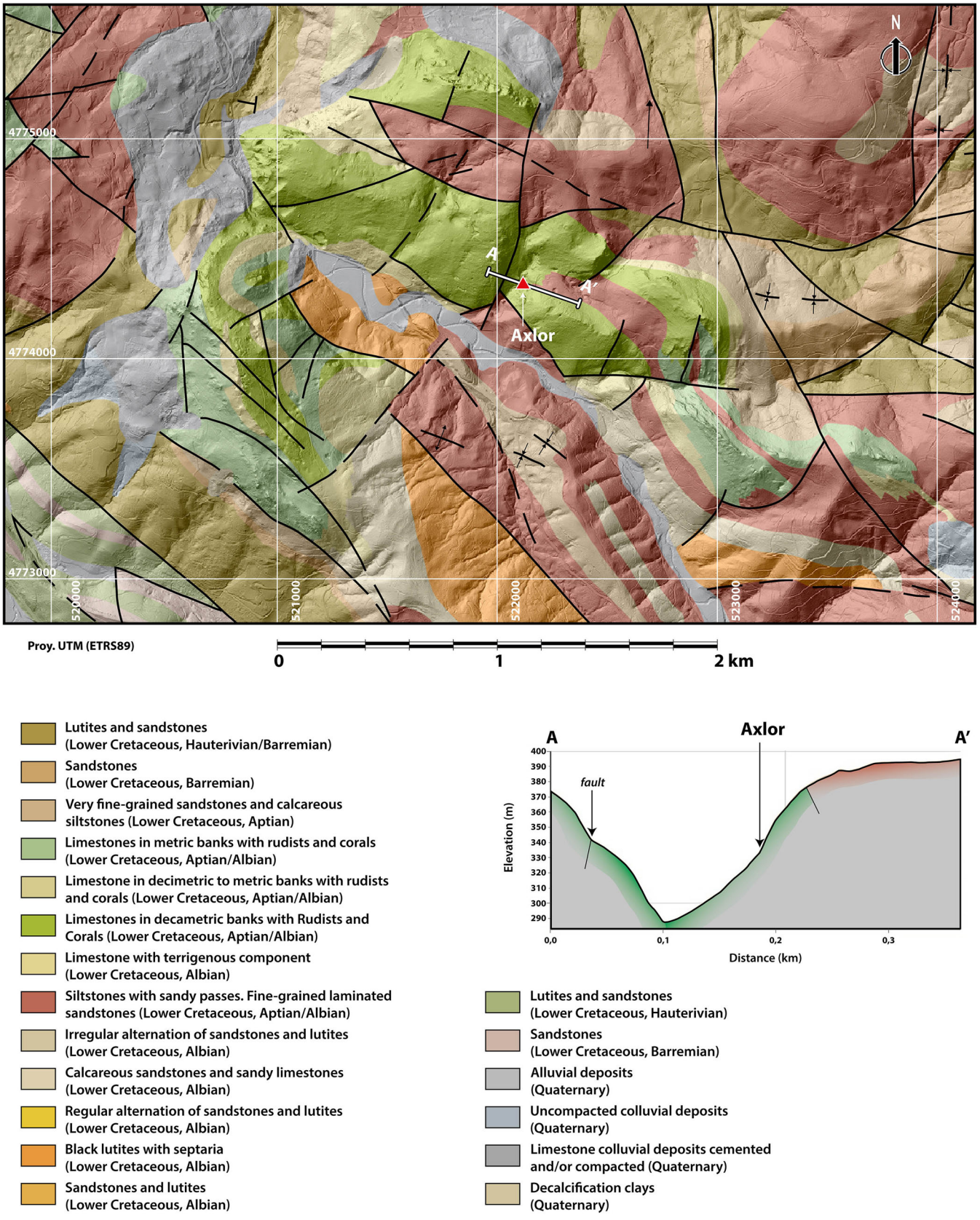

Figure 2. Geological and lithological map of the Axlor environment. Cross-section of the immediate valley, with indication of the lithological outcrops. [Color figure can be viewed at wileyonlinelibrary.com]

Level C ranges between 15 and 20 cm in thickness and is composed of fine ochre-coloured materials, marginally lower proportion of clays and silts (78.2%), and small calcareous gravels. The granulometric distribution curve of level C differs when compared to the rest of the profile because of a higher proportion of coarse elements. The proportion of coarse sands increases compared to level B (15.7% of the total sand fraction), although the fine sand fraction remains more significant, with the mode and median in the class 0.125–0.08 mm (Fig. S4). The medium sands of level C also exhibit greater wear, with a predominance of sub-angular grains and >10% of grains being rounded. This reveals slightly

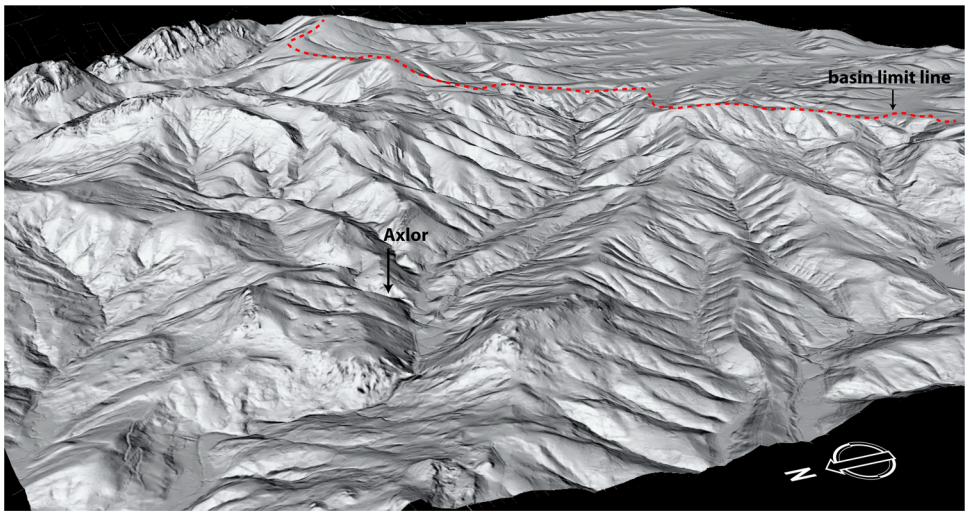

Figure 3. Digital terrain model of the Arratia valley from the NW. The red dotted line indicates the border between the Atlantic and Mediterranean basins. [Color figure can be viewed at wileyonlinelibrary.com]

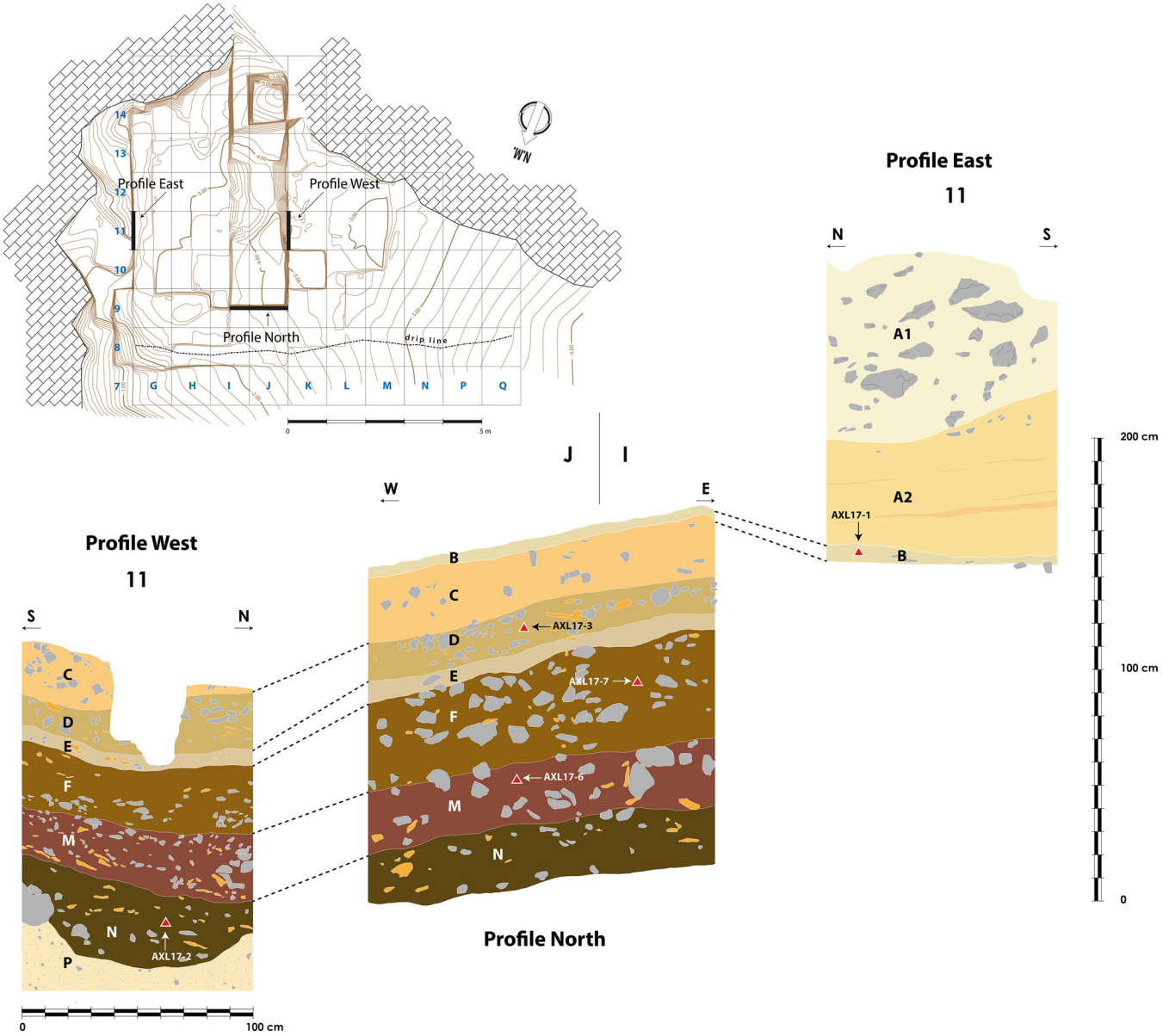

Figure 4. Stratigraphy of the Middle Palaeolithic sequence in Axlor. Red triangles show the position of OSL samples. [Color figure can be viewed at wileyonlinelibrary.com]

more energetic transport conditions compared to those of the upper levels. The density of lithic (1700–2600 m^{-3}) and faunal remains is lower than in level B, but both assemblages retain similar compositions across the two levels.

Level D ranges between 10 and 20 cm in thickness and forms a very dense bone deposit. The sedimentary matrix is composed predominantly of fines, with silts and clays making up almost 80%. The sands are dominated by the fine sand fraction, with a mode and median in the 0.125–0.08-mm class, giving the granulometric distribution curve a logarithmic aspect, similar to that of level B (Fig. S4). The medium sands show a slightly higher level of wear and, although there is a significant proportion of sub-angular grains (~40%), a similar or slightly higher proportion corresponds to sub-rounded grains, with some rounded and well-rounded elements preserved. Both the granulometry and wear attributes reflect distinctive depositional energy conditions, probably characterized by limited but continuous water flow regimes that allowed shaping of the grain surfaces (especially quartz). More than 97 400 fragments of bone larger than 4 mm have been recovered. The faunal assemblage is mainly composed of *Bison* and *Cervus*, with lower amounts of *Capra* and *Equus*. The lithic industry of level D is typically Quina, with abundant scrapers (see Fig. S10) and resharpening flakes transformed into new tools by retouching (González-Urquijo et al., 2005; Lazuén and González-Urquijo, 2015). The industry in level D is manufactured mainly from exogenous flint (>30 km distance; 70% of the raw material used), but also includes local lutite and quartz. There is no evidence of *in situ* knapping and the flakes are highly exploited, which makes it difficult to ascertain the techniques used in the production of these flakes. There is evidence for a cycle of intense resharpening of the Quina sidescrapers, using hammers on diaphyseal splinters of *Cervus* and large bovids, followed by intensive use of the resulting flakes, which are often retouched (Mozota Holgueras, 2014, González Urquijo et al., 2014).

Level E is 5 cm thick and made up of yellowish clays, with small contributions of centimetre-sized limestone clasts in some parts of the deposit. This level contains relatively scarce archaeological remains.

Level F progressively becomes wedged towards the interior of the cavity, changing in thickness from 25–40 cm in the northern sector to 20 cm in the south. Clasts are present as small blocks, boulders and angular gravels, in an abundant matrix of fines (77% silts and clays) that exhibit clear gradation from bottom to top. The sand fraction maintains a predominance of fine sands (76.9% of the total sand fraction), although it is somewhat coarser (mode and median are in the 0.2–0.125-mm class) than in overlying levels (Fig. S4). This level differs from the overlying deposits due to the increased shaping of sand grains, with rounded and sub-rounded grain proportion amounting to ~50%. This probably indicates the predominance of a low-energy flow regime, which facilitated decantation and deposition of clays and silts, but with occasional higher energy flow events.

Level M is around 25 cm thick and comprises an abundant fine sediment matrix with infrequent clasts, pebbles and gravels. The fine grain fraction of level M (71% silts and clays) represents the lowest proportion for the entire stratigraphic sequence. The sand fraction continues to be dominated by the fine class (almost 60% of the total sand fraction) with a modal value in the 0.2–0.125-mm range, though medium-sized sands gain more significance compared to all other levels (35.3% of the total sand fraction) (Fig. S4). The sand grains, essentially quartz, are well defined by their sub-angularity, which clearly predominates over sub-rounded grain types. This suggests limited transport distances for the sediment matrix, with limestone clasts additionally being sporadically incorporated from the cave walls.

The archaeological composition of levels M and F are currently under examination and will be published in upcoming studies. Preliminary studies of the lithic industry show intermediate characteristics when compared to those of levels N and D. This implies the presence of Levallois knapping and the dominance of flat supports, but also the presence of some thick sidescrapers.

Level N constitutes the base of the Mousterian sequence. The thickness of level N varies widely depending on the location; in the outermost area the thickness exceeds 40 cm. Level N has a very dark colour, ranging from dark brown to dark grey. Micromorphological studies show the presence of charred plants, which include mainly branches and leaves, as well as tar fragments (Lambrecht et al., 2021; Rodríguez de Vera et al., 2020). Silts and clays predominate (86.3%), while coarse sands exhibit particularly limited abundance (only 3.7% of the sand fraction). The sand grains generally show angular and sub-angular surface textures, although they also exhibit a secondary tendency towards rounded morphologies, which is a sign of their external (allochthonous) origins. A significant proportion of the sediment is of anthropic origin with an important contribution from macrofaunal remains (more than 237 700 pieces larger than 4 mm have been recovered), composed mostly of *Cervus* (~75% of the identified remains). Level N includes abundant macro carbonaceous remains and combustion structures in different degrees of conservation. The lithic industry is very abundant (>20 000 m^{-3}) and is made up of tools knapped on flint, quartz and mudstone. Technologically, the industry is defined by the presence of a characteristic micro-Levallois knapping system and an appreciable amount of Mousterian points (González-Urquijo, et al., 2006).

Level P lies immediately below level N and was formed by an accumulation of large limestone blocks, sometimes metre-sized, with a matrix of yellowish quartzite clay, probably of colluvial origin. Level P is the only archaeologically sterile level. Levels R and S are located in the inner cave's section and do not form part of this study.

It is important to note that correlation between the original stratigraphic scheme of Barandiarán (Barandiarán, 1980) and the more recent stratigraphic scheme developed during the 21st century excavations (adopted herein) is extremely complicated. This is partly because during the 1967–1974 studies the levels were excavated horizontally, without due consideration for the slight dipping plane affecting the deposits (Lazuen and González-Urquijo, 2020). This resulted in the conflation of archaeological materials from layers that are now considered distinctive. For example, some sections of level V in the old scheme contain materials from levels D, E, F, M and N in the recent classification system. For this reason, no direct association or clear correspondence can be established between the former and current stratigraphic schemes (see Supporting Information for further discussions).

Methods

Optical dating approach, sample collection and laboratory preparation

The optical dating study at Axlor is focused on single-grain quartz OSL analyses in order to gain maximum insights into any potential methodological complications that could have affected optical dating reliability in this cave setting; in particular, the presence of insufficiently bleached grain

populations (e.g. Arnold et al., 2008; 2009), contaminant grains associated with syn- or post-depositional mixing (e.g. Arnold et al., 2013, 2019, 2011), and aberrant grains displaying inherently unsuitable luminescence properties (e.g. Demuro et al., 2008; 2013). Single-grain TT-OSL dating of quartz (e.g. Arnold et al., 2014; Demuro et al., 2015; 2019b), which exhibits significantly higher dose saturation limits than conventional quartz OSL (e.g. Arnold et al., 2015), was additionally applied to the oldest sample collected from the Axlor sequence as a means of cross-checking the reliability of the OSL dating approach over the natural dose ranges of these samples (150–200 Gy). TT-OSL dating was applied to individual grains of quartz rather than multi-grain aliquots in this study, following the reliable application of this approach at similar archaeological settings across the Iberian Peninsula and neighbouring regions (e.g. Arnold et al., 2014, 2015; Demuro et al., 2014, 2015, 2019a, 2019b, 2020).

Five optical dating samples were collected from the sedimentary sequence at Axlor (Figure 5). One sample was collected from each of the following units (from the base upwards): level N (AXL17-2), level M (AXL17-6), level F (AXL17-7), level D (AXL17-3) and level B (AXL17-1). Level E was not sampled because the layer was too thin to accommodate the width of the sampling tube without cross-cutting adjacent layers. Samples were collected by inserting PVC tubes horizontally into clean refreshed profiles, and were immediately sealed with black plastic and duct tape upon extraction to avoid exposure to daylight. Additional sediment was collected from within 1 cm of each sample position for water content and dosimetry evaluations.

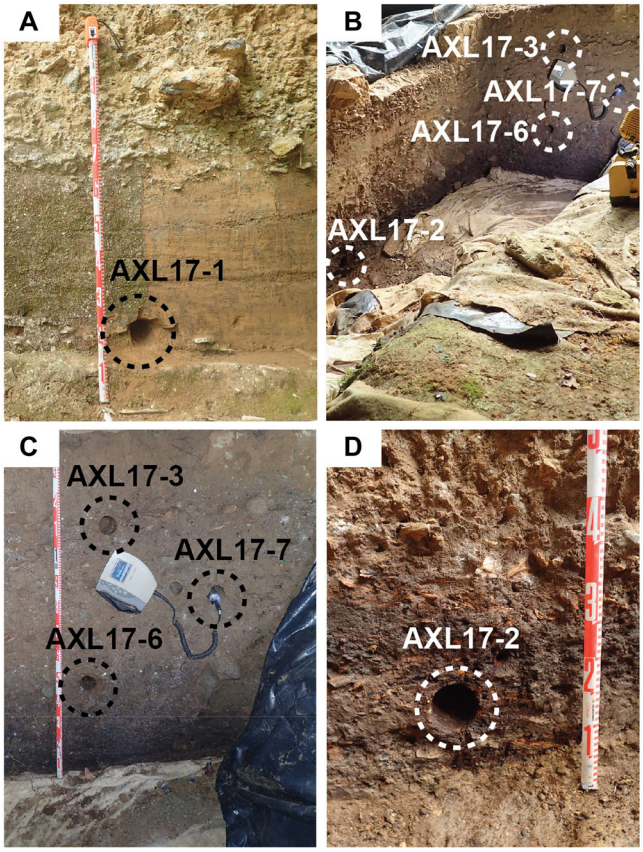

Figure 5. Images showing OSL sample positions at Axlor (corresponding to the holes within the dashed circles). (A) The stratigraphically highest sample (AXL17-1) collected from level B on the western exposure. (B) Overview of OSL samples collected from the main external excavation area. (C) Close up of OSL sample positions in levels M (AXL17-6), F (AXL17-7) and D (AXL17-3). (D) Detail of close up of the OSL sample (AXL17-2) position in level N. [Color figure can be viewed at wileyonlinelibrary.com]

Purified coarse-grained quartz fractions were extracted from the luminescence samples under safe light (dim red LED) conditions at the University of Adelaide, and prepared for burial dose estimation following established procedures (Aitken, 1998). The 212–250-μm quartz fractions of all samples were prepared for single-grain OSL measurements, and the 90–125-μm quartz fraction of sample AXL17-2 was additionally prepared for single-grain TT-OSL measurements. Samples were initially wet sieved to extract the 90–350-μm fine sand fraction, and treated with hydrogen peroxide (H_2O_2) and hydrochloric acid (HCl) to eliminate organics and carbonates, respectively. The quartz fraction was subsequently isolated from lighter feldspars, clays and heavy minerals using heavy liquid (LST lithium heteropolytungstate) densities of 2.62 and 2.72 g cm^{-3}. The 212–250-μm quartz fractions of all samples, plus the 90–125-μm quartz fraction of sample AXL17-2, were then sieved out and etched for 40 min using 48% HF to remove the alpha-irradiated outer layer of the quartz extracts. The etched grains were finally rinsed in 30% HCl to remove any precipitated fluorides and re-sieved using a 63-μm sieve to eliminate any disaggregated grains.

Dose rate determination

Environmental dose rates (Tables 1 and 2) have been determined using a combination of *in situ* field gamma spectrometry and low-level beta counting. High-resolution gamma spectrometry (HRGS) measurements have additionally been undertaken to determine the state of secular equilibrium in the ^{238}U and ^{232}Th decay series. Field gamma spectrometry measurements were made with a Canberra NaI:Tl detector and analysed using the 'energy windows' method to determine individual K, U and Th elemental concentrations (Arnold et al., 2012b; Duval and Arnold, 2013). External beta dose rates were calculated from measurements made on a Risø GM-25-5 beta counter, using homogenized sediment sub-samples collected from the main luminescence dating sample positions. Final beta dose rate estimates were calculated after making allowance for beta dose attenuation due to grain-size effects and HF etching (Brennan, 2003; Mejdahl, 1979). The conversion factors of Guérin et al. (2011) were used to derive gamma and beta dose rates from the measured radionuclide concentrations and specific activities. Cosmic-ray dose rates were calculated after taking into consideration site altitude, geomagnetic latitude, and density, thickness and geometry of sediment overburden, as described in Prescott and Hutton (1994). The effects of bedrock shielding were additionally incorporated into the cosmic dose rate calculation using the integrated $\cos^2\phi$-zenith angular dependence procedures outlined in Allkofer (1974) and Smith et al. (1997). The beta, gamma and cosmic-ray dose rates were corrected for long-term sediment moisture contents following the procedures outlined in Aitken (1985) and Readhead (1987). The present-day moisture contents of the Axlor samples range between 17 and 34% of dry weight. These values are considered to be representative of moisture conditions prevailing throughout the sample burial period because the cave environment remains sufficiently well protected from major variations in external atmospheric conditions. A relative 1σ uncertainty of 20% has been assigned to the long-term moisture estimates of all samples to accommodate any minor variations during burial.

Equivalent dose (D_e) evaluation

OSL and TT-OSL equivalent dose (D_e) measurements were made using Risø TL/OSL-DA-20 readers equipped with either EMI 9235QB or Electron Tubes PDM 9107B photomultiplier

Table 1. Environmental dose rate summary for the single-grain quartz OSL and TT-OSL samples from Axlor.

Sample	Grain Size (μm)	Sample depth (cm)	Water content (%)[a]	Environmental dose rate (Gy ka^{-1})				
				Gamma[b]	Beta[c]	Cosmic[d]	Internal[e]	Total[f]
AXL17-1	212–250	230	17.5	1.32 ± 0.04	2.07 ± 0.10	0.06 ± 0.01	0.03 ± 0.01	3.48 ± 0.19
AXL17-3	212–250	265	24.8	1.00 ± 0.03	1.44 ± 0.07	0.05 ± 0.01	0.03 ± 0.01	2.53 ± 0.15
AXL17-7	212–250	300	17.6	0.82 ± 0.03	1.63 ± 0.08	0.05 ± 0.01	0.03 ± 0.01	2.53 ± 0.14
AXL17-6	212–250	335	25.8	0.75 ± 0.03	1.24 ± 0.06	0.05 ± 0.01	0.03 ± 0.01	2.07 ± 0.13
AXL17-2	212–250	390	33.7	0.61 ± 0.02	0.83 ± 0.04	0.04 ± 0.01	0.03 ± 0.01	1.52 ± 0.11
AXL17-2	90–125	390	33.7	0.61 ± 0.02	0.89 ± 0.05	0.04 ± 0.01	0.03 ± 0.01	1.58 ± 0.11

[a]Field water content is expressed as percentage of dry mass of mineral fraction and assigned relative uncertainties of ±20%.
[b]Gamma dose rates were calculated from *in situ* field gamma spectrometry measurements made at each sample position with a NaI:Tl detector, using the 'energy windows' approach (Arnold et al., 2012b; Duval & Arnold, 2013).
[c]Beta dose rates were calculated on dried and powdered sediment samples using a Risø GM-25-5 low-level beta counter (Bøtter-Jensen and Mejdahl, 1988), after making allowance for beta dose attenuation due to grain-size effects and HF etching (Brennan, 2003).
[d]Cosmic-ray dose rates were calculated using the approach of Prescott and Hutton (1994) and assigned a relative uncertainty of ±10%.
[e]An internal dose rate of 0.03 Gy ka^{-1}, with an assigned relative uncertainty of ±30%, has been adopted for these samples based on intrinsic ^{238}U and ^{232}Th contents published by Mejdahl (1987), Bowler et al. (2003), Jacobs et al. (2006), Pawley et al. (2008) and Lewis et al. (2020), and an a-value of 0.04 ± 0.01 (Rees-Jones, 1995; Rees-Jones & Tite, 1997).
[f]Mean ± total uncertainty (68% confidence interval), calculated as the quadratic sum of the random and systematic uncertainties.

Table 2. High-resolution gamma spectrometry (HRGS) results for the Axlor optical dating samples.

Sample	Radionuclide specific activities (Bq kg^{-1})[a,b]						Beta dose rate (Gy ka^{-1})[c]	Daughter:parent isotopic ratio		
	^{238}U	^{226}Ra	^{210}Pb	^{228}Ra	^{228}Th	^{40}K		^{226}Ra:^{238}U	^{210}Pb:^{226}Ra	^{228}Th:^{228}Ra
AXL17-1	64.1 ± 2.5	64.7 ± 0.9	59.5 ± 3.3	57.6 ± 1.3	58.7 ± 1.3	623 ± 15	1.91 ± 0.08	1.03 ± 0.04	0.91 ± 0.05	1.02 ± 0.03
AXL17-3	75.9 ± 2.9	74.2 ± 1.0	67.1 ± 4.0	46.4 ± 1.2	45.6 ± 1.1	426 ± 11	1.47 ± 0.07	0.98 ± 0.04	0.91 ± 0.06	0.98 ± 0.04
AXL17-7	49.7 ± 3.7	57.1 ± 0.9	53.7 ± 3.5	52.2 ± 1.4	53.2 ± 1.3	492 ± 13	1.57 ± 0.07	1.15 ± 0.09	0.94 ± 0.06	1.02 ± 0.04
AXL17-6	64.3 ± 2.9	63.6 ± 0.9	53.4 ± 3.1	41.3 ± 1.1	40.7 ± 1.0	364 ± 9	1.21 ± 0.06	0.99 ± 0.05	0.84 ± 0.05	0.99 ± 0.04
AXL17-2	44.9 ± 2.8	54.6 ± 0.9	48.0 ± 3.4	31.3 ± 1.3	31.1 ± 1.0	272 ± 9	0.87 ± 0.04	1.22 ± 0.08	0.88 ± 0.06	0.99 ± 0.05

[a]Measurements made on dried and powdered sediment sub-samples of ~8 g.
[b]Mean ± total uncertainty (68% confidence interval), calculated as the quadratic sum of the random and systematic uncertainties.
[c]Beta dose rates are shown for comparison with the results obtained on the same bulk sediment samples using low-level beta counting (shown in Table 1). The beta dose rate estimates have been calculated for the 212–250-μm quartz fractions used for OSL dating, making allowance for beta dose attenuation due to sediment moisture content (see Table 1), grain-size effects and HF etching. Radionuclide concentrations and specific activities have been converted to dose rates using the conversion factors given in Guérin et al. (2011).

tubes, and spatially calibrated ^{90}Sr/^{90}Y β sources delivering mean dose rates of between ~6.7 and ~8.5 Gy min^{-1}. Single-grain OSL and TT-OSL signals were stimulated with 10-mW Nd:YVO4 single-grain laser attachments emitting at 532 nm (maximum power of ~50 W cm^{-2}). Multi-grain OSL signals (i.e. dose recovery test measurements) were stimulated using blue LEDs (470 nm, maximum power 52–102 W cm^{-2}), while infrared signals (necessary for the detection of contaminant feldspar grains) were stimulated with infrared LEDs (peak emission 850 or 870 nm, maximum power of 141–349 W cm^{-2}). Single-grain OSL and TT-OSL UV emissions were detected through 7.5-mm-thick U-340 Hoya filters.

Single-grain OSL and TT-OSL D_e measurements were made by carefully brushing 212–250- or 90–125-μm quartz grains into standard single-grain aluminium discs drilled with an array of 300 × 300-μm holes. For TT-OSL measurements made using the 90–125-μm quartz fractions, it is expected that ~18 grains were placed in each grain-hole position of the single-grain discs (Arnold et al., 2012a). This measurement configuration was chosen because it has been shown that cave deposits in northern Spain typically contain relatively low proportions of TT-OSL-producing quartz grains (e.g. Arnold et al., 2014; Demuro et al., 2014; 2019a; 2019b); this approach therefore offers a practical means of enhancing the number of usable D_e values per disc while minimizing any 'pseudo' single-grain averaging effects. For sample AXL17-2, the vast majority (79%) of grain-hole positions measured using this pseudo-single-grain approach still produced statistically indistinguishable or very dim TT-OSL signals (see 'Single-grain OSL signal characteristics'), which suggests close approximation to true single-grain resolution and minimal influences of multi-grain averaging effects (Demuro et al., 2013).

Single-grain OSL and TT-OSL D_e values have been obtained using the single-aliquot regenerative-dose (SAR) protocols described in Murray and Wintle (2000) and Stevens et al. (2009), which have been modified to measure individual grains following Demuro et al. (2015) (Table 3). These protocols were found to be optimal for the measurement of quartz grains from Axlor, as determined through SAR validation tests (i.e. dose recovery tests) (see Supporting Information).

Sensitivity-corrected OSL and TT-OSL responses were constructed from the first 0.09 and 0.17 s of green laser stimulation, respectively, with a background subtraction derived from the last 0.25 s of stimulation. Individual D_e values were calculated after interpolating the sensitivity-corrected natural signals (L_n/T_n) onto their corresponding sensitivity-corrected regenerative dose (L_x/T_x) response curves; the latter have been fitted with a single saturating exponential function for all OSL and TT-OSL measurements. Individual D_e uncertainties (presented at 1σ) comprise three sources of error: (i) a random uncertainty term arising from photon-counting statistics for each OSL measurement, calculated using equation 3 of Galbraith (2002); (ii) an

Table 3. SAR protocols used in this study to undertake dose recovery tests on multi-grain aliquots (protocol A) and to obtain single-grain OSL (protocol B) and single-grain TT-OSL (protocol C) ages from quartz. L_n and L_x refer to the natural and regenerative-dose signal measurements, respectively. T_n and T_x refer to the test dose signals measured after the L_n and L_x signals, respectively.

	Multi-grain OSL SAR protocol			Single-grain OSL SAR protocol			Single-grain TT-OSL SAR protocol	
A Step	Treatment	Symbol	B Step	Treatment	Symbol	C Step	Treatment	Symbol
1[a]	Give dose		1[a]	Give dose		1[a]	Give dose	
2	Stimulate with infrared diodes at 50°C for 60s (90% power)		2[b]	Stimulate with infrared diodes at 50°C for 60s (50% power)		2	Preheat to 260°C for 10s	PH1
3	Preheat to either 200, 220, 240 or 260°C for 10s	PH1	3	Preheat to 220°C for 10s	PH1	3	Stimulate with green laser at 125°C for 2s (90% power)	
4	Stimulate with blue LEDs at 125°C for 60s (90% power)	L_n or L_x	4	Stimulate with green laser at 125°C for 2s (90% power)	L_n or L_x	4	Preheat to 260°C for 10s	PH2
5	Give test dose		5	Give test dose		5	Stimulate with green laser at 125°C for 3s (90% power)	L_n or L_x
6	Stimulate with infrared diodes at 50°C for 60s (90% power)		6	Preheat to 160°C for 10s	PH2	6	Stimulate with blue LEDs at 280°C for 400s	
7	Preheat to 160 or 200°C for 10s	PH2	7	Stimulate with green laser at 125°C for 2s (90% power)	T_n or T_x	7	Give test dose	
8	Stimulate with blue LEDs at 125°C for 60s (90% power)	T_n or T_x	8	Return to 1		8	Preheat to 260°C for 10s	PH3
9	Return to 1					9	Stimulate with green laser at 125°C for 2s (90% power)	
						10	Preheat to 260°C for 10s	PH4
						11	Stimulate with green laser at 125°C for 3s (90% power)	T_n or T_x
						12	Stimulate with blue LEDs at 290°C for 400s	
						13	Return to 1	

[a]Step omitted when measuring the natural signal (L_n).
[b]Step added only when measuring the IR depletion ratio described in Duller (2003).

empirically determined instrument-reproducibility uncertainty of 1.5–1.9% for each single-grain measurement, calculated specifically for the readers used in this study; and (iii) a dose–response curve fitting uncertainty determined using 1000 iterations of the Monte Carlo method described by Duller (2007) and implemented in Analyst.

Single-grain OSL and TT-OSL D_e values were not included in the final age calculations if they exhibited one or more of the following properties: (i) the net intensity of the natural test dose signal, T_n, was $<3\sigma$ above the late-light background signal; (ii) the low-dose recycling ratio (plus high-dose recycling ratio in the case of single-grain OSL) was not consistent with unity at 2σ [i.e. the ratio of sensitivity-corrected luminescence responses (L_x/T_x) for two identical regenerative doses]; (iii) the OSL infrared (IR) depletion ratio of Duller (2003) was not consistent with unity at 2σ (i.e. the ratio of the L_x/T_x values obtained for two identical regenerative doses measured with and without prior IR stimulation, designed to detect feldspar contamination or inclusions); (iv) the recuperation ratio, calculated as the ratio of the sensitivity-corrected 0-Gy dose point (L_0/T_x) to the sensitivity-corrected natural (L_n/T_n), was >5%; (v) the net T_n signal had a relative error of >30%; (vi) the sensitivity-corrected natural signal (L_n/T_n) did not intercept the sensitivity-corrected dose–response curve; (vii) the dose–response curve displayed anomalous properties (i.e. zero or negative response with increasing dose) or very scattered L_x/T_x values that could not be successfully fitted with the Monte Carlo procedure and, hence, did not yield finite D_e values and uncertainty ranges; and (viii) the L_n/T_n value intercepted the saturated part of the dose–response curve [L_n/T_n values were statistically indistinguishable from the saturation limit (I_{max}) of the dose–response curve at 2σ]. For TT-OSL D_e estimation, criterion (iii) (feldspar contamination) was checked by measuring the OSL IR depletion ratio separately and in the standard manner for single-grain OSL measurements, i.e. by measuring two conventional single-grain OSL SAR cycles (as opposed to two single-grain TT-OSL SAR cycles) with and without IR stimulation.

Results

Environmental dose rates

The results of the optical dating dose rate evaluations are summarized in Tables 1 and 2. The total dose rates for levels B to N range between 1.52 and 3.48 Gy ka^{-1} (Table 1), with most of the variability being driven by differences in sediment ^{40}K activities and limestone clast abundance between layers (Table 2). The grain-size-attenuated and moisture-corrected beta dose rates calculated using the HRGS results (Table 2) are consistent with those determined for each sample using low-level beta counting (Table 1), confirming the reliability of our dose rate estimates.

The HRGS daughter–parent isotopic ratios for ^{238}U, ^{226}Ra, ^{210}Pb, ^{228}Ra and ^{228}Th are generally consistent with unity at either 1σ or 2σ for the six optical dating samples, indicating that their ^{238}U and ^{232}Th chains are in, or close to, present-day secular equilibrium (Table 2). The two exceptions to this trend are sample AXL17-6, which exhibits minor disequilibrium in the lower part of the ^{238}U decay chain (^{210}Pb:^{226}Ra ratio of 0.84 ± 0.05), and sample AXL17-2, which exhibits minor disequilibrium in the upper part of the ^{238}U decay chain (^{226}Ra:^{238}U ratio of 1.22 ± 0.08). These two instances of disequilibria are not considered to have a significant effect on the final dose rate estimates because (i) the ^{238}U decay series only contributes 37–39% to the total quartz dose rates of samples AXL17-6 and AXL17-2 (calculated using the HGRS results), and (ii) dosimetry modelling undertaken elsewhere has demonstrated that isotopic disequilibria of similar magnitudes are only likely to give rise to minor deviations (<5%) in long-term dose rate estimates (e.g. Olley et al., 1996; Olley et al., 1997; Preusser and Degering, 2007); such systematic biases would be significantly less than the existing 2σ uncertainty ranges on our final dose rate estimates. Indeed, adjusting the ^{210}Pb activity of AXL17-6 so that it equates to the measured ^{226}Ra activity of this sample (i.e. fixing the ^{210}Pb:^{226}Ra ratio to unity) changes the final dose rate by <1%. Similarly, adjusting the ^{226}Ra activity of AXL17-2 so that it equates to the measured ^{238}U activity of this sample (i.e. fixing the ^{226}Ra:^{238}U ratio to unity) changes the final dose rate by 5.2%.

Single-grain OSL signal characteristics

The total number of grains measured for single-grain OSL D_e estimation varied between 4500 and 9100 per sample, and ~1–5% of these grains passed the SAR rejection criteria and were used for the final age calculations (Table 4). The vast majority of grains were rejected due to poor OSL signal sensitivity (~71–82% of grains displayed $L_n < 3\sigma$ above background and net T_n errors >30%) (Table 4). A similar proportion of the 1000 pseudo single-grain TT-OSL measurements made on AXL17-2 were rejected due to poor signal sensitivity (~79%), confirming that they probably approximated true single-grain resolution. A slightly higher proportion of TT-OSL D_e measurements passed the SAR rejection criteria (8%) and were considered suitable for dating in comparison to the OSL D_e datasets. This is primarily attributable to the absence of saturated grains and signal contributions from feldspar contaminants for the TT-OSL D_e dataset (Table 4).

Representative decay and dose–response curves for the single-grain OSL and TT-OSL signals that satisfied the SAR quality assurance criteria are shown in Figure 6. The OSL signal brightness of the Axlor quartz is generally moderate to weak, with the brightest 1% of grains yielding 15–850 net counts Gy^{-1} in the first 0.09 s of stimulation (Figure 6a). Samples AXL17-1, AXL17-3 and AXL17-7, which come from upper site deposits (levels B–F), display lower overall OSL signal intensities compared to samples AXL17-6 and AXL17-2 from the lower site deposits (levels M and N) (Figure 6a). These differences in inherent quartz signal brightness may reflect changes in sediment sourcing between the upper and lower levels, or different thermal annealing histories related to anthropic combustion activities in levels M and N. The measured OSL signals of accepted grains are fast-decaying (generally being depleted to background levels within 0.5 s of stimulation), consistent with quartz signals dominated by the most readily bleached (so-called 'fast') OSL component (Figure 6b). The single-grain TT-OSL signals of sample AXL17-2 display similar rapid decay rates (Figure 6c), consistent with charge transfer into the most readily bleached OSL dating trap. However, the TT-OSL signal intensities are much weaker than their OSL counterparts, typically by an order of magnitude, as has been reported elsewhere for Iberian quartz (e.g. Demuro et al., 2015; 2019a; 2019b) (Figure 6b,c). The single-grain TT-OSL dose–response curves exhibit very high saturation dose limits, with characteristic saturation dose (D_0 values) typically on the order of 300 to >1000 Gy (Figure 6c).

D_e estimates

In general, the single-grain OSL and TT-OSL D_e distributions of the Axlor samples are consistent with well-bleached, unmixed

Table 4. Single-grain OSL and TT-OSL classification statistics showing proportion of rejected and accepted grains after applying the SAR quality assurance criteria to the natural D_e measurements and dose–recovery test measurements. These criteria were applied to each single-grain measurement in the order listed. T_n = natural test dose signal response; L_n/T_n = sensitivity-corrected natural signal response; DRC = dose response curve; BG = background signal.

		Rejected grains (%)									
Sample/measurement type	Grains measured (*n*)	T_n signal <3×BG	Poor low recycling ratio	Poor high recycling ratio	IR depletion ratio	Recuperation >5%	Net T_n error >30%	L_n/T_n not intercepting DRC	Anomalous dose–response curve	Saturated	Accepted grains (%)
D_e estimation											
AXL17-1 (OSL)	4500	57.1	10.0	4.9	5.5	0.4	17.3	0.5	1.0	0.9	2.4
AXL17-3 (OSL)	5500	61.4	7.4	4.3	5.8	1.0	15.7	0.4	1.2	0.8	2.1
AXL17-7 (OSL)	9100	71.0	6.6	3.3	4.3	0.3	11.1	0.5	0.9	0.6	1.4
AXL17-6 (OSL)	6200	67.6	7.7	4.2	3.5	0.2	9.3	1.0	2.1	2.2	2.3
AXL17-2 (OSL)	6100	59.9	9.4	4.3	4.1	0.3	10.5	2.3	2.2	2.2	4.9
AXL17-2 (TT-OSL)	1000	43.9	10.3	-	0	0	35.3	0.1	2.1	0	8.3
Dose recovery tests (OSL)											
AXL17-6 (given dose = 50 Gy)	1700	75.5	8.8	2.7	2.1	0	5.6	0.2	1.3	0	3.8
AXL17-6 (given dose = 150 Gy)	1500	71.7	8.7	3.3	2.7	0	6.4	0.6	1.6	1.5	3.5
AXL17-2 (given dose = 150 Gy)	1600	54.7	8.7	4.9	5.0	0.4	14.4	0.4	2.1	2.2	7.1

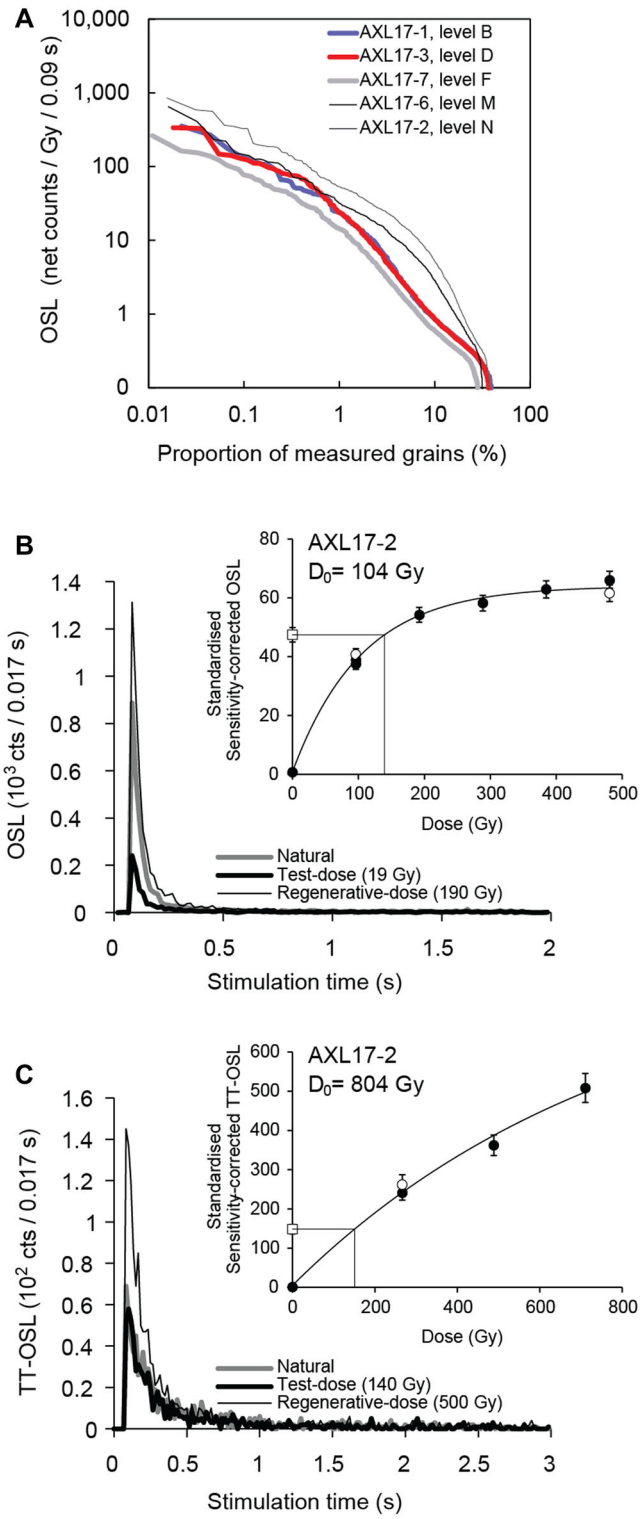

Figure 6. (A) OSL signal brightness distribution showing net T_n signal intensities of individual grains (expressed as counts per Gy per 0.09 s) ranked from brightest to dimmest and plotted against cumulative proportion of measured grains. The data shown are for single-grain OSL measurements made using the 212–250-μm quartz fraction for all samples from Axlor. Examples of (B) OSL and (C) TT-OSL decay curves and sensitivity-corrected dose–response curves (inset) for two representative quartz grains of sample AXL17-2. White square denotes the sensitivity-corrected natural OSL signal; filled circles denote the sensitivity-corrected regenerative dose OSL signals; white circles denote the repeated regenerative dose points used to calculate the recycling ratios. The D_0 value characterizes the rate of signal saturation with respect to administered dose and equates to the dose value for which the saturating exponential dose–response curve slope is 1/*e* (or ~0.37) of its initial value. [Color figure can be viewed at wileyonlinelibrary.com]

sediments (e.g. Arnold et al., 2008; 2016; Jacobs et al., 2016; Doerschner et al., 2019; Arnold and Roberts, 2009; Bailey and Arnold, 2006; Jankowski et al., 2020). The single-grain OSL D_e datasets for samples AXL17-1, AXL17-3, AXL17-6 and AXL17-2, and the single-grain TT-OSL D_e dataset for sample AXL17-2, display relatively limited D_e dispersion that is reasonably well represented by the weighted mean value (as indicated by the large proportions of grains lying within the 2σ grey bands of the radial plots) (Figure 7), and low overdispersion values ranging between 22 ± 3 and 28 ± 6% (Table 5). These overdispersion values are consistent with (i.e. within 2σ of) those typically reported for well-bleached and undisturbed single-grain D_e datasets (e.g. Arnold et al., 2019; Arnold and Roberts, 2009) and they are comparable to, albeit systematically higher than, the 2σ overdispersion ranges obtained in the high dose recovery tests for samples AXL17-6 and AXL17-2 (2–22%). Three of these five D_e datasets (AXL17-2 TT-OSL, AXL17-6 OSL and AXL17-3 OSL) are considered to be normally distributed according to the weighted skewness test outlined by Bailey and Arnold (2006) and Arnold and Roberts (2011), while the remaining two D_e datasets are classified as moderately negatively skewed (AXL17-1 OSL) and slightly positively skewed (AXL17-2 OSL) (Table 5). Application of the maximum log likelihood (L_{max}) test (Arnold et al., 2009) indicates that the central age model (CAM) is statistically favoured over the three- or four-parameter minimum age models (MAM-3 or MAM-4) of Galbraith et al. (1999) for all D_e datasets (Table 5).

Sample AXL17-7 from level F exhibits a more heterogeneous single-grain OSL D_e distribution in comparison to the other samples from the site (Figure 7). This sample is characterized by a larger proportion of individual D_e values lying outside of the weighted mean burial dose 2σ range, and a moderate overdispersion value of 37 ± 4% (Table 5). Despite the enhanced D_e scatter, AXL17-7 does not display a prominent leading-edge of low D_e values or asymmetric tail of higher D_e values, and is therefore not consistent with D_e characteristics commonly reported for heterogeneously bleached single-grain OSL samples (e.g. Arnold et al., 2007; Bailey and Arnold, 2006; Olley et al., 1999). This sample is considered to be significantly negatively skewed when compared with its 2σ critical skewness scores (Table 5), while the L_{max} test (Arnold et al., 2009) indicates that the CAM is statistically favoured over the MAM-3 or MAM-4, as is the case for all other D_e datasets from the site.

Collectively, these single-grain OSL and TT-OSL D_e characteristics suggest that the Axlor samples do not suffer from major extrinsic D_e scatter related to insufficient bleaching prior to burial (e.g. Arnold et al., 2008; 2011), syn-depositional mixing with pre-existing cave deposits prior to burial (e.g. Arnold et al., 2019; Ruiz et al., 2021; Zilhão et al., 2020), or widespread post-depositional sediment mixing between units (e.g. Arnold et al., 2013). It seems likely that the low to moderate overdispersion observed for these samples is attributable to intrinsic experimental scatter not captured by the dose recovery test (e.g. Galbraith et al., 2005; Jacobs et al., 2006; Demuro et al., 2013; Arnold et al., 2013) and extrinsic field-related scatter associated with beta-dose spatial heterogeneity (e.g. Nathan et al., 2003; Arnold et al., 2014; Guérin et al., 2015a; Martin et al., 2015; Smedley et al., 2020). We have therefore used the weighted mean (CAM) D_e values to derive the final OSL and TT-OSL burial dose estimates for all samples, in accordance with the L_{max} test results (Arnold et al., 2009). For comparative purposes, we also present the D_e values and ages obtained for these samples using an alternative

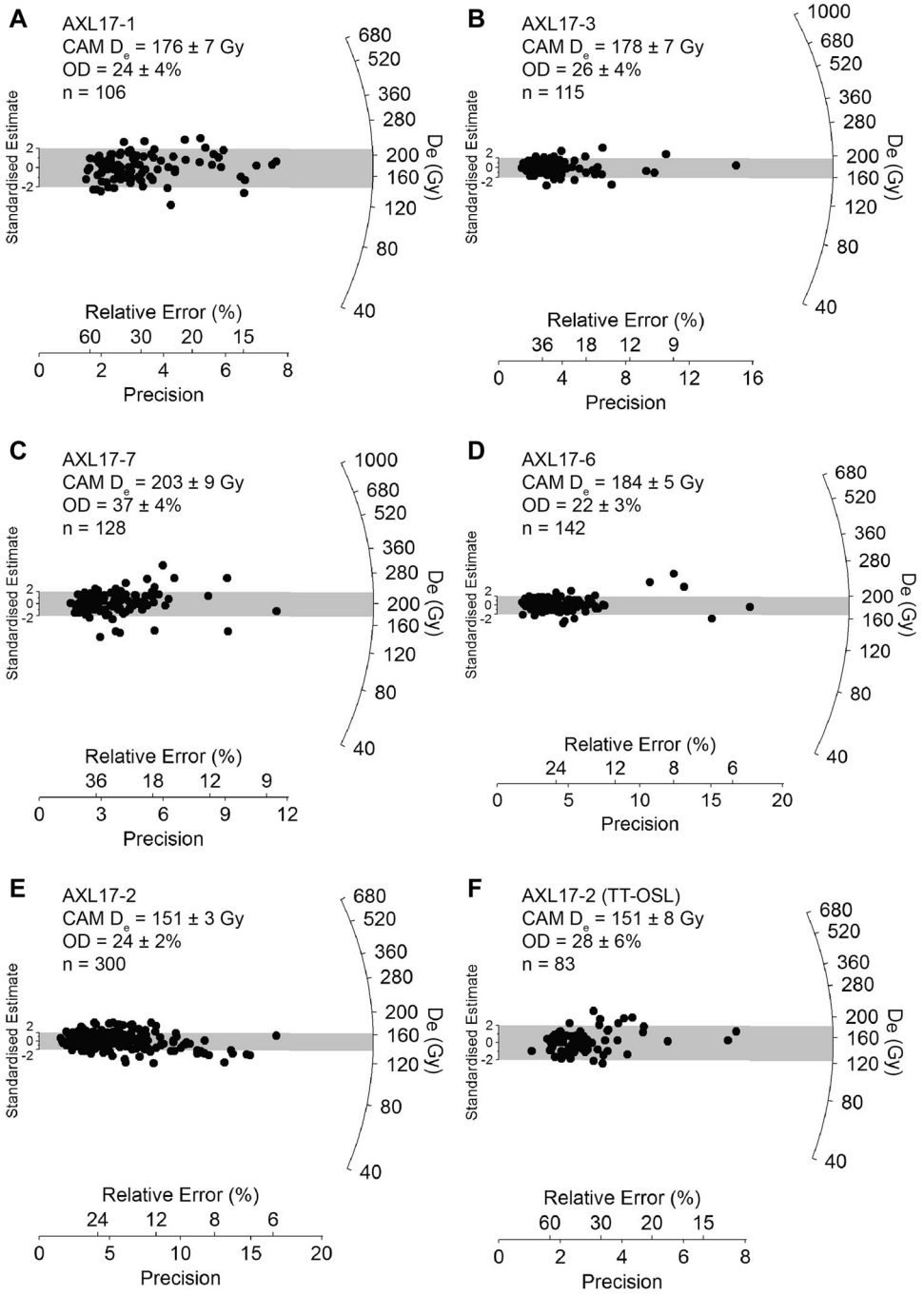

Figure 7. Single-grain OSL D_e distributions for the (A–E) OSL and (F) TT-OSL samples dated in this study, shown as radial plots. The grey bands are centred on the D_e values used for the age calculations, which were derived using the central age model of Galbraith et al. (1999).

measure of central tendency in the Supporting Information (the average dose model or ADM of Guérin et al., 2017), and discuss potential practical considerations of using this alternative age model with our D_e datasets. In all cases tested, the ADM and CAM ages are statistically indistinguishable at 1σ (average difference in ADM and CAM ages for all comparative datasets is only 2.6%; Table S5), confirming that our final chronological interpretations are not unduly influenced by the choice of weighted mean D_e estimates.

The weighted mean D_e values for the single-grain OSL datasets range between ~150 and ~200 Gy, and produce stratigraphically coherent ages for level N (base of the external Middle Palaeolithic sequence) to level B (top of the Middle Palaeolithic sequence) (Table 5). Encouragingly, the replicate single-grain TT-OSL D_e value for level N (150.8 ± 7.9 Gy) is consistent with the corresponding OSL D_e value at 1σ (151.4 ± 2.9 Gy). This outcome suggests that the accepted grain populations of the single-grain OSL datasets have sufficiently high dose saturation limits to ensure finite and reliable D_e estimation over the natural burial dose ranges of these deposits. However, to examine potential single-grain OSL dose saturation effects more explicitly, we analysed the characteristic saturation dose (D_0) value for each accepted grain of sample AXL17-2 (calculated using a single saturating exponential dose–response curve fit). The resulting weighted mean (CAM) D_0 value for AXL17-2 is ~129 Gy, which is sufficiently high to enable finite D_e determination over the expected burial dose range for this sample (i.e. ~150 Gy; as determined from the semi-independent TT-OSL dating results). To explore the issue further, we applied the 2×D_0 acceptance threshold criterion (Arnold et al., 2016; Demuro et al., 2019a; Demuro et al., 2015) to the accepted grains of a subset of

Table 5. D_e summary statistics, age model results, and corresponding single-grain OSL and TT-OSL ages for the Axlor samples. The total dose rates shown have been calculated using a combination of *in situ* gamma-ray spectrometry and low-level beta counting measurements. The preferred age for each sample is indicated with an asterisk.

Sample	Sample depth (cm)	Level	Grain size (μm)	Total dose rate (Gy ka^{-1})	Accepted/ measured	Overdispersion (%)	Weighted skewness	Critical skewness (95% CI)[a]	Critical skewness (68% CI)[a]	Age model[b,c]	L_{max} score[d]	D_e (Gy)[e]	Age (ka)[e,f]
AXL17-1	230	B	212–250	3.48 ± 0.19	106/4500	24 ± 4	−0.582	0.475	0.237	CAM	−59.843	176.2 ± 6.8	50.7 ± 3.5*
										MAM-3	−59.98	84.1 ± 4.2	44.5 ± 6.4
										MAM-4	−59.555	85.5 ± 4.2	26.7 ± 16.5
AXL17-3	265	D	212–250	2.53 ± 0.15	115/5500	26 ± 4	−0.202	0.456	0.228	CAM	−66.304	178.1 ± 7.0	70.4 ± 5.3*
										MAM-3	−66.417	146.3 ± 18.9	57.8 ± 8.3
										MAM-4	−66.272	77.3 ± 66.0	30.6 ± 26.2
AXL17-7	300	F	212–250	2.53 ± 0.14	128/9100	37 ± 4	−0.637	0.433	0.216	CAM	−88.33	202.6 ± 8.6	80.0 ± 5.8*
										MAM-3	−92.56	100.0 ± 10.5	39.5 ± 4.8
										MAM-4	−85.57	82.4 ± 15.1	32.6 ± 6.3
AXL17-6	335	M	212–250	2.07 ± 0.13	142/6200	22 ± 3	−0.299	0.411	0.205	CAM	−50.918	184.2 ± 5.3	89.0 ± 6.5*
										MAM-3	−50.857	175.9 ± 16.9	85.0 ± 9.9
										MAM-4	−50.807	178.6 ± 65.0	86.3 ± 31.9
AXL17-2	390	N	212–250	1.52 ± 0.11	300/6100	24 ± 2	0.297	0.282	0.141	CAM	−113.647	151.4 ± 2.9	99.6 ± 7.6*
										MAM-3	−112.202	139.6 ± 8.2	91.8 ± 8.7
										MAM-4	−111.862	142.3 ± 5.6	93.6 ± 7.9
AXL17-2 (TT-OSL)	390	N	90–125	1.58 ± 0.11	83/1000	28 ± 6	0.100	0.537	0.268	CAM	−55.628	150.8 ± 7.9	95.6 ± 8.7*
										MAM-3	−55.361	133.1 ± 22.7	84.4 ± 15.7
										MAM-4	−55.277	138.4 ± 39.2	87.7 ± 25.7

[a]Weighted skewness scores have been calculated on log-transformed D_e values using eq. 7-8 of Arnold and Roberts (2009). Critical skewness scores have been calculated using eq. 16 of Bailey and Arnold (2006). Critical skewness values are taken to be equivalent to twice the standard error of skewness score (95% CI) for single-grain D_e datasets, following the results of sensitivity analyses performed by Bailey and Arnold (2006) and Arnold et al. (2007).

[b]CAM = central age model; MAM-3 = three-parameter minimum age model; MAM-4 = four-parameter minimum age model (Galbraith et al., 1999).

[c]MAM D_e estimates have been calculated after adding, in quadrature, a relative error (σ_b value) of 20% to each individual D_e measurement error to approximate the site-specific baseline (best-case scenario) overdispersion observed in well-bleached and unmixed sedimentary samples from this site (i.e. AXL17-6). This underlying dose overdispersion value is consistent with the average published value of 20 ± 1% reported for well-bleached and unmixed samples by Arnold and Roberts (2009).

[d]Maximum log likelihood score of the CAM, MAM-3 or MAM-4 fit. For a given sample, the L_{max} score of the MAM-3 is expected to be substantially higher (i.e. at least 1.92-fold greater) than that of the CAM when the addition of the extra model parameter improves the fit to the data. Likewise, the L_{max} score of the MAM-4 is expected to be significantly greater than that of the MAM-3 (by at least 1.92 when compared with the 95% CI of a χ^2 distribution) when the addition of the extra model parameter improves the fit to the data. If the extra parameter of the MAM-3 (or MAM-4) is not supported by the data, then its L_{max} score will be similar to (i.e. within 1.92 of) the CAM (or MAM-3) L_{max} score, indicating that the simpler age model explains the data equally well (Arnold et al., 2009).

[e]Mean ± total uncertainty (68% CI), calculated as the quadratic sum of the random and systematic uncertainties. Total uncertainty includes a systematic component of ±2% associated with laboratory beta-source calibration.

[f]The preferred age for each sample is indicated with an asterisk. For these samples, the preferred age has been derived using the statistical age model that yielded the optimum L_{max} score, following the criterion outlined in footnote[d] and Arnold et al. (2009).

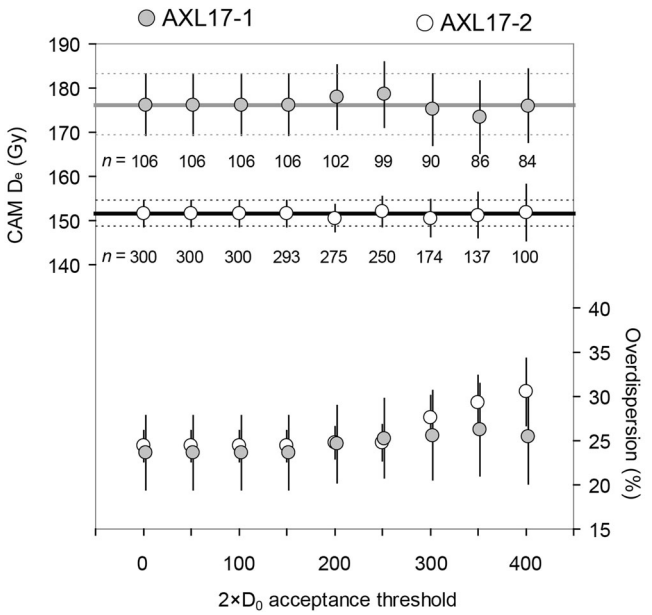

Figure 8. Single-grain weighted mean (central age model; CAM) D_e and overdispersion values for the natural D_e dataset of AXL17-1 and AXL17-2 after applying the $2\times D_0$ acceptance threshold criterion of Demuro et al. (2015) (D_e errors are shown at 1σ). In these plots, progressively higher $2\times D_0$ thresholds have been applied to the D_e datasets, starting with a $2\times D_0$ threshold of 0 and increasing the $2\times D_0$ threshold in increments of 50. In each instance, grains were only accepted for further D_e analysis if their individual $2\times D_0$ value equalled or exceeded the corresponding threshold shown on the *x*-axis at 2σ (for details see Arnold et al., 2016). The number of accepted grains remaining after applying progressively higher $2\times D_0$ thresholds is shown for each dataset. The grey and black horizontal lines represent the starting CAM D_e value of samples AXL17-1 and AXL17-2, respectively.

samples. Samples AXL17-2 and AXL17-1 were chosen for this sensitivity analysis because they provide good stratigraphic coverage and are representative of the D_e ranges obtained with the Axlor OSL dataset. The $2\times D_0$ acceptance threshold criterion ensures only grains with $2\times D_0$ values higher than a specific burial dose are accepted for final D_e estimation. Grains that produce unrealistically low D_e values purely as a result of insufficient dose saturation limits are therefore excluded from the final burial dose evaluation, providing a means to evaluate potential age underestimation effects arising from inherently unsuitable grains. Application of progressively higher $2\times D_0$ threshold values from 50 to 400 Gy (increasing in 50-Gy increments) did not significantly change the weighted mean D_e or overdispersion values of these samples at 2σ (Figure 8). These results add further confidence to our interpretation that dose–response curve saturation of the OSL signal has not negatively affected the ages obtained for the Axlor samples.

Single-grain OSL and TT-OSL ages

The single-grain OSL ages obtained for the external sequence at Axlor range between ~100 and ~50 ka (ages marked with an asterisk in Table 5). The lower part of the sedimentary sequence, which encompasses levels N, M and F, is dated to 99.6 ± 7.6 ka (AXL17-2), 89.0 ± 6.5 ka (AXL17-6) and 80.0 ± 5.8 ka (AXL17-7), respectively (Table 5). The overlying levels D and B yield ages of 70.4 ± 5.3 ka (AXL17-3) and 50.7 ± 3.5 ka (AXL17-1), respectively (Table 5). The single-grain TT-OSL age of 95.6 ± 8.7 ka for AXL17-2 (level N) is statistically consistent with the corresponding single-grain OSL age (Table 5), providing good support for the reliability of the optical dating procedures employed in this study. The parity between the replicate results for AXL17-2 supports the findings of several recent studies where OSL and TT-OSL have been applied in tandem at Late Pleistocene cave sites (e.g. Arnold et al., 2019; Demuro et al., 2019a), and suggests that the single-grain TT-OSL signals of allochthonous sediments can be sufficiently reset prior to transportation and deposition in some cave settings (despite the relatively slow bleaching rates). In such instances, single-grain TT-OSL can offer a useful means of cross-checking dating reliability for Late Pleistocene deposits that may be approaching the limits of conventional OSL dating.

Discussion

Chronology of the Axlor Middle Palaeolithic sequence

The combined single-grain OSL and TT-OSL chronologies obtained in this study reveal that Axlor levels N, M and F probably accumulated during marine isotope stage (MIS) 5d–a (109–82 ka; Lisiecki and Raymo, 2005), while levels D to B probably accumulated within the period encompassing the start of MIS 4 (71–57 ka) through to the beginning or middle of MIS 3 (57–29 ka) (Figure 9). The new single-grain OSL ages are consistent with (i.e. older than) the previously published *terminus ante quem* ^{14}C ages for the site (minimum age estimates of >42.9 ka; Table S1), and suggest that the Middle Palaeolithic sequence accumulated during a protracted period lasting ~50 kyr. Importantly, our optical dating results provide independent confirmation that the previously obtained ^{14}C ages for Axlor should be considered as minimum ages only. They also serve as an important example of how Middle Palaeolithic sites that exhibit interstratified mixtures of infinite,

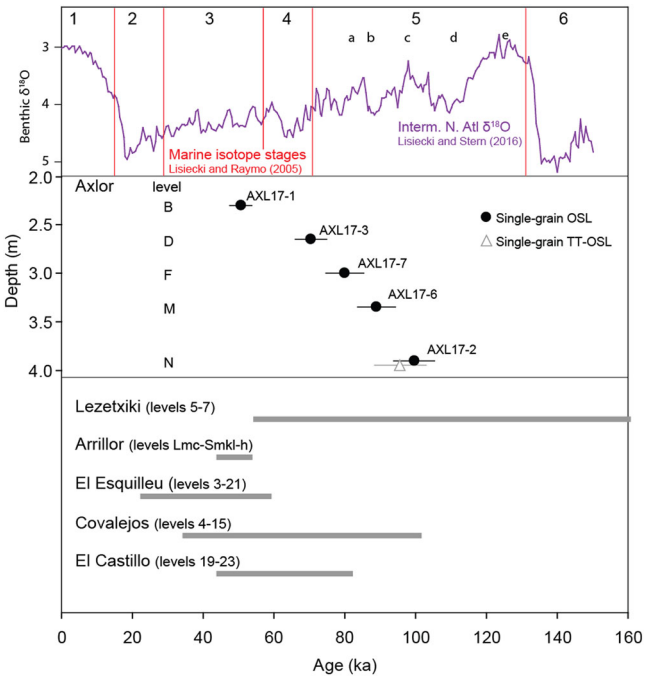

Figure 9. Single-grain OSL ages (and associated 1σ errors) for the five luminescence samples collected from Axlor (black circles), plotted against the δ^{18}O isotope curve for the last glacial cycle (Intermediate North Atlantic records; Lisiecki and Stern, 2016) and marine isotope stages (MIS) (Lisiecki and Raymo, 2005). Also shown is the single-grain TT-OSL age obtained for sample AXL17-2 (white triangle) and age ranges of main Middle Palaeolithic records located in the North Atlantic Iberian region and neighbouring areas (based on the published dating results shown in Table 6). [Color figure can be viewed at wileyonlinelibrary.com]

finite and young outlying ^{14}C ages may be diagnostic of otherwise undetected inaccuracies related to incomplete removal of exogenous carbon. This is particularly relevant where standard acid–base–acid ^{14}C pre-treatment procedures have been employed on bone samples that are close to or beyond the limits of the ^{14}C technique, as is the case at Axlor.

Single-grain OSL dating studies undertaken at several other Iberian Middle Palaeolithic sites that were once considered to represent late Neanderthal occupations have revealed similarly older chronologies in comparison to initial ^{14}C dating evaluations. This is the case, for instance, at the MIS 5–4 site of Galería de las Estatuas (Demuro et al., 2019a), and to some extent the MIS 4–3 site of Hotel California (Arnold et al., 2013), both located in or around the Atapuerca karst system (northern Spain), as well as the Portuguese sites of Gruta da Oliveira and Figuera Brava (Zilhão et al., 2020; 2021a). At most of these sites, the OSL chronologies are older than their ^{14}C counterparts by several tens of thousand years, with the reliability of the OSL re-evaluations being independently verified by other radiometric techniques that are equally applicable beyond ^{14}C dating limits [e.g. U-series dating of speleothems; Vernot et al., 2021; combined electron spin resonance (ESR) U-series dating of fossil teeth]. The results of the present study confirm that Axlor can be added to the list of Iberian Middle Palaeolithic sites where single-grain OSL dating re-evaluations have revealed much earlier (MIS 5, MIS 4 and early- to mid-MIS 3) Neanderthal occupations than originally inferred from ^{14}C datasets.

In spite of the dating disparities at these sites, it should be emphasized that single-grain OSL dating results obtained at many other Iberian Middle Palaeolithic sites have confirmed the validity of the mid-MIS 3 Neanderthal chronologies originally established by ^{14}C studies. This is the case, for instance, at Prado Vargas (northern Spain), Roca dels Bous (Pre-Pyrenees ranges), Cova del Gegant (Cataluña) and Caldeirão (Portugal) (Benito-Calvo et al., 2020; Daura et al., 2021; Ruiz et al., 2021; Zilhão et al., 2021b), where single-grain OSL ages of 40–45 ka for layers containing Middle Palaeolithic tools and Neanderthal remains (in the case of Prado Vargas) are in agreement at 1σ or 2σ with corresponding ^{14}C chronologies. These favourable comparison studies are just as important as the aforementioned negative case studies in highlighting the usefulness of luminescence dating for cross-checking existing MIS 3 ^{14}C results at key Neanderthal fossil and cultural sites across the region. Single-grain OSL dating has an important role to play in corroborating and refining current understanding of Neanderthal histories across southwest Europe, perhaps all the more so given that recent applications of compound-specific ^{14}C dating appear to show that even rigorous ^{14}C preparation techniques such as ultrafiltration may not necessarily be sufficient to completely remove contaminants in some dating contexts (e.g. Devièse et al., 2021; Spindler et al., 2021).

The broader significance of the new chronological results for Axlor is highlighted by Table 6, which provides a synthesis of dated Middle Palaeolithic sites from the North Atlantic Iberian region and the immediately adjacent regions of northern Iberia. In total, 25 other Middle Palaeolithic sites have chronological frameworks derived as part of detailed site studies or dedicated dating evaluations. It is worth noting that some of the published studies shown in Table 6 lack sufficient experimental details to enable meaningful evaluations of dating reliability (e.g. El Esquilleu, Cueva Millán, La Ermita, Hundidero), or provide preliminary dating results (e.g. Guérin and Lahaye, 2022), while others have only involved dating of a single sample (e.g. La Mina and Askondo) or single stratigraphic layer (e.g. Prado Vargas, Cueva Corazon, Cueva Millán). Most of the dated Middle Palaeolithic sites from the region have been chronologically constrained wholly or partly using ^{14}C approaches (19 of the 27 sites in Table 6), with OSL/thermoluminescence (TL) dating having been used at ten sites, U-series dating being employed at seven sites, ESR dating being used at five sites and amino acid racemization (AAR) employed at five sites. As a result of this reliance on ^{14}C dating, only ten sites (including Axlor) from the region have well-established, finite chronological frameworks extending beyond 55 ka, meaning that our current understanding of Neanderthal occupation dynamics across northern Iberia is fragmentary and primarily limited to late surviving populations.

When compared with this regional chronological synthesis, Axlor represents one of the few well-dated, long-range Middle Palaeolithic sequences for the north Atlantic Iberian region, and therefore constitutes an important chronostratigraphic reference for examining Neanderthal cultural change and adaptations to environmental change between MIS 5 and early- to mid-MIS 3. Additional chronological studies of other Neanderthal sites are now needed to elucidate the longer term population geographies, behavioural adaptations and cultural dynamics of the Middle Palaeolithic on a regional scale. As borne out by the present study, single-grain OSL dating is well placed to extend and expand the temporal coverage of existing chronological frameworks, particularly when employed as part of multi-technique dating evaluations that target complementary materials at Middle Palaeolithic sites.

Indicators of palaeoenvironmental change at Axlor

As noted in the 'Stratigraphy' section and the Supporting Information, the lower levels of the Axlor sequence (M-F) are dominated by deer remains (~75%), while the faunal composition of the upper levels (D–B) reveals a distinct increase in the frequency of large bovid and horse remains (González-Urquijo, et al., 2006). The change in composition of the large mammal assemblage between the lower and upper levels has been interpreted as indicative of a shift in environmental conditions, though the accumulation of the various faunal remains at the site is interpreted as being mainly anthropogenic (Castaños, 2005; González-Urquijo, et al., 2005).

The new ages obtained for the Axlor exterior sequence allow us to refine these interpretations, as the timing of this faunal shift suggests it coincides with broader climatic deterioration associated with the transition between interglacial and glacial stages. The ages obtained for level N reveals it probably formed during the MIS 5 interglacial complex, which was characterized regionally by the development of a mixed temperate forest (Daniau et al., 2009; Gómez-Orellana et al., 2007; Sánchez Goñi et al., 2008). The MIS 5 attribution of level N is reinforced by the dominance of red deer in the faunal assemblage (Castaños, 2005), a key indicator of deciduous and mixed woodland ecosystems, and the incorporation of woodland vegetation remains in the form of branches and leaves (Lambrecht et al., 2021; Rodríguez de Vera et al., 2020).

In contrast to these temperate climate proxies, the palaeoenvironmental indicators of level D reveal much harsher climatic conditions, consistent with an age attribution to MIS 4 based on the highest probability OSL age range. The fauna of this level is dominated by taxa that reflect more open landscapes (high frequencies of large bovids and horses) (González-Urquijo, et al., 2006), with pollen studies revealing a landscape dominated by grasses and heathers with patchy evergreen–boreal forest (Daniau et al., 2009; Gómez-Orellana et al., 2007). The chronological, faunal, pollen and micromorphology evidence therefore consistently points to an

Table 6. Regional synthesis of well-known Middle Palaeolithic sites from the North Atlantic Iberian region and adjacent regions.

Site	Region	Site type	Level (in stratigraphic order; top to bottom)	Material/sample	Age (ka)[a]	Age (^{14}C BP)[b]	Calibrated age range (cal BP)[c]	Method[d]	Reference(s)
North Atlantic Iberian region									
Axlor	Dima, Biscay	Cave	B	Bone (Beta-203108)		42.7 ± 0.9	44.1–47.4	AMS ^{14}C ABA	(González-Urquijo et al., 2021)
			B	Sed. quartz grains (AXL17-1)	50.7 ± 3.5 (1σ)		42.9–47.7	Single-grain OSL	This study
			D	Bone (Beta-144262)		42.0 ± 1.3	44.6–54.8	AMS ^{14}C ABA	(González-Urquijo et al., 2005)
			D	Bone (Beta-203107)			>43.0	AMS ^{14}C ABA	(González-Urquijo et al., 2021)
			D	Bone (Beta-225486)			37.0–39.2	AMS ^{14}C ABA	(Frías, 2013)
			D	Sed. quartz grains (AXL17-3)	70.4 ± 5.3 (1σ)	44.9 ± 1.9	>47.5	Single-grain OSL	This study
			F	Bone (Beta-225485)		>43.0		AMS ^{14}C ABA	(Frías, 2013)
			F	Bone (Beta-225487)				AMS ^{14}C ABA	(Frías, 2013)
			F	Sed. quartz grains (AXL17-7)	80.0 ± 5.8 (1σ)	33.3 ± 0.4		Single-grain OSL	This study
			M	Sed. quartz grains (AXL17-6)	89.0 ± 6.5 (1σ)	>47.5		Single-grain OSL	This study
			N	Sed. quartz grains (AXL17-2)	99.6 ± 7.6 (1σ)			Single-grain OSL	This study
			N	Sed. quartz grains (AXL17-2)	95.6 ± 8.7 (1σ)			Single-grain TT-OSL	This study
Arlanpe	Lemoa, Biscay	Cave	SQ3	LEB10457	70.6			AAR	(Rios-Garaizar et al., 2015)
			SQ1 (top)	ICTJA-4711	184.2 + 34.6/−26.6			U/Th	(Rios-Garaizar et al., 2015)
Askondo	Mañaria, Biscay	Cave	12	Bone (Beta-313144)		>41.4	>41.4	AMS ^{14}C	(Garcia-Ibaibarriaga et al., 2015)
Lezetxiki I	Arrasate, Gipuzkoa	Cave	V	Bone (IPH-Lz 13)	130 ± 17			ESR	(Falguères et al., 2005)
			V	Bone (IPH-Lz 1)	57 ± 2			U/Th (Alpha spectrometry)	(Falguères et al., 2005)
			V	Bone (IPH-Lz 2)	70 ± 9			U/Th (Gamma spectrometry)	(Falguères et al., 2005)
			V	Bone (IPH-Lz 3)	186 + 164/−6			U/Th (Gamma spectrometry)	(Falguères et al., 2005)
			VI	Bone (IPH-Lz 14)	234 ± 32			ESR	(Falguères et al., 2005)
			VI	Bone (IPH-Lz 4)	288 + 34/−26			U/Th (Alpha spectrometry)	(Falguères et al., 2005)
			VI	Bone (IPH-Lz 5)	231 + 92/−49			U/Th (Gamma spectrometry)	(Falguères et al., 2005)
			VI	Bone (IPH-Lz 6)	200 + 129/−58			U/Th (Gamma spectrometry)	(Falguères et al., 2005)
			VII	Bone (IPH-Lz 15)	225 ± 40			ESR	(Falguères et al., 2005)
			VII	Bone (IPH-Lz 7)	140 ± 6			U/Th (Alpha spectrometry)	(Falguères et al., 2005)

(*Continued*)

Table 6. (*Continued*)

Site	Region	Site type	Level (in stratigraphic order; top to bottom)	Material/sample	Age (ka)[a]	Age (^{14}C BP)[b]	Calibrated age range (cal BP)[c]	Method[d]	Reference(s)
			VII	Bone (IPH-Lz 8)	115 + 9/−8			U/Th (Alpha spectrometry)	(Falguères et al., 2005)
			VII	Bone (IPH-Lz 9)	121 ± 4			U/Th (Gamma spectrometry)	(Falguères et al., 2005)
			VII	Bone (IPH-Lz 10)	129 + 24/−20			U/Th (Alpha spectrometry)	(Falguères et al., 2005)
			VII	Bone (IPH-Lz 11)	200 + 142/−52			U/Th (Gamma spectrometry)	(Falguères et al., 2005)
			VII	Bone (IPH-Lz 12)	>260			U/Th (Gamma spectrometry)	(Falguères et al., 2005)
Amalda I	Zestoa, Gipuzkoa	Cave	VII	Bone (OxA-32500)		44.5 ± 2.1	44.4–54.9	AMS ^{14}C ultrafiltration	(Marín-Arroyo et al., 2018)
				Bone (OxA-34933)		42.6 ± 1.6	42.9–49.9	AMS ^{14}C ultrafiltration	(Marín-Arroyo et al., 2018)
El Esquilleu	Cillorigo de Liébana, Cantabria	Cave	3	Bone (AA-29664)		40.7 ± 2.3	41.7–52.1	AMS ^{14}C ABA	(Baena et al., 2005)
			3	Bone (OxA-19967)		19.3 ± 0.1	23.0–23.7	AMS ^{14}C ultrafiltration	(Maroto et al., 2012)
			3	Bone (OxA-19968)		19.3 ± 0.1	23.0–23.7	AMS ^{14}C ultrafiltration	(Maroto et al., 2012)
			3	Charcoal (GrA-33829)		3.6 ± 0.1	3.6–4.2	AMS ^{14}C acid only	(Maroto et al., 2012)
			3b	Bone (OxA-19246)		20.8 ± 0.1	24.7–25.3	AMS ^{14}C ultrafiltration	(Maroto et al., 2012)
			4	Charcoal (GrA-35064)		22.8 ± 0.5	25.0–27.9	AMS ^{14}C acid only	(Maroto et al., 2012)
			5	Charcoal (GrA-35065)		30.3 ± 0.1	34.4–35.1	AMS ^{14}C acid only	(Maroto et al., 2012)
			6	Bone (OxA-19965)		43.7 ± 1.4	44.1–50.3	AMS ^{14}C ultrafiltration	(Maroto et al., 2012)
			6	Bone (OxA-19966)		44.1 ± 1.3	44.5–50.2	AMS ^{14}C ultrafiltration	(Maroto et al., 2012)
			6	Charcoal (GrA-33816)		40.1 ± 0.5	42.7–44.3	AMS ^{14}C ABA	(Maroto et al., 2012)
			6f	Charcoal (AA-37883)		34.4 ± 0.7	37.6–41.0	AMS ^{14}C ABA	(Baena et al., 2005)
			11f	Charcoal (AA-37882)		36.5 ± 0.7	40.4–42.3	AMS ^{14}C ABA	(Baena et al., 2005)
			13	Charcoal (Beta - 149320)		39.0 ± 0.3	42.4–42.9	AMS ^{14}C ABA	(Baena et al., 2005)
			17	Charcoal (OxA-20318)		53.4 ± 0.9	51.8–55.5	AMS ^{14}C ABOX-SC	(Maroto et al., 2012)
			17	Charcoal (OxA-20319)		>58.5	>58.5	AMS ^{14}C ABOX-SC	(Maroto et al., 2012)
			17	Charcoal (OxA-X-2297-31)		49.4 ± 1.3	>50.0	AMS ^{14}C ABOX-SC	(Maroto et al., 2012)
			17	Charcoal (OxA-20320)		52.6 ± 1.2	50.5–55.5	AMS ^{14}C ABOX-SC	(Maroto et al., 2012)
			17	Charcoal (OxA-19993)		>54.0	>54.0	AMS ^{14}C ABOX-SC	(Maroto et al., 2012)
			18	Charcoal (OxA-11414)		49.7 ± 1.6	49.8–>55.0	AMS ^{14}C ABA	(Baena et al., 2005)
			19	Charcoal (OxA-19085)		39.3 ± 0.3	42.5–43.1	AMS ^{14}C ABA	(Maroto et al., 2012)
			19	Charcoal (OxA-19086)		>54.6	>54.6	AMS ^{14}C ABOX-SC	(Maroto et al., 2012)
			19	Charcoal (OxA-V-2284-29)		39.6 ± 0.4	42.5–43.9	AMS ^{14}C Plasma oxidation	(Maroto et al., 2012)

(*Continued*)

Table 6. (*Continued*)

Site	Region	Site type	Level (in stratigraphic order; top to bottom)	Material/sample	Age (ka)[a]	Age (^{14}C BP)[b]	Calibrated age range (cal BP)[c]	Method[d]	Reference(s)
			19	Charcoal (OxA-V-2284-30)		39.7 ± 0.5	42.5–44.0	AMS ^{14}C Plasma oxidation	(Maroto et al., 2012)
			21-I	Charcoal (OxA-20321)		>59.6	>59.6	AMS ^{14}C ABOX-SC	(Maroto et al., 2012)
			21d	Burnt clay (Mad3299)	51.0 ± 5.1			TL	(Baena et al., 2005)
			21b	Burnt clay (Mad3300)	53.5 ± 5.1			TL	(Baena et al., 2005)
Covalejos	Camargo, Cantabria	Cave	4 (D)	?		40.7 ± 2.3	41.7–52.1	AMS ^{14}C ABA	(Sanguino et al., 2005)
			4 (D)	?		41.6 ± 0.7	43.2–45.6	AMS ^{14}C ABA	(Sanguino et al., 2005)
			4 (D)	Bone (GrA-33811)		43.1 ± 0.6	44.6–46.8	AMS ^{14}C Longin (improved)	(Maroto et al., 2012)
			4	Sed. quartz grains (COV 4)	35.7 ± 2.1 (1σ)				Guérin and Lahaye (2022)
			5	Sed. quartz grains (COV 5)	43.8 ± 2.5 (1σ)			Single-grain OSL	Guérin and Lahaye (2022)
			6	Sed. quartz grains (COV 6B)	49.2 ± 2.5 (1σ)			Single-grain OSL	Guérin and Lahaye (2022)
			7	Sed. quartz grains (COV 7)	52.5 ± 3.1 (1σ)			Single-grain OSL	Guérin and Lahaye (2022)
			7 (I)	Bone (GrA-33822)		30.9 ± 0.3	34.6–36.0	Single-grain OSL	(Maroto et al., 2012)
			8 (J)	Bone (GrA-33812)		>45.0	>45.0	AMS ^{14}C Longin (improved)	(Maroto et al., 2012)
			8 (J)	Hearth	38.3 ± 3.6			AMS ^{14}C Longin (improved)	(Sanguino et al., 2005)
			8	Sed. quartz grains (COV 8)	49.0 ± 3.9 (1σ)			TL	Guérin and Lahaye (2022)
			9	Sed. quartz grains (COV 9)	64.1 ± 4.1 (1σ)			Single-grain OSL	Guérin and Lahaye (2022)
			11	Sed. quartz grains (COV 11)	93.0 ± 8.1 (1σ)			Single-grain OSL	Guérin and Lahaye (2022)
			12 (N)	Speleothem	91.9 ± 4.0			Single-grain OSL	(Sanguino et al., 2005)
			15 (Q)	Speleothem	101			U/Th	(Sanguino et al., 2005)
			15	Sed. quartz grains (COV 15)	84.3 ± 4.7 (1σ)			U/Th Single-grain OSL	Guérin and Lahaye (2022)
El Castillo	Puente Viesgo, Cantabria	Cave	19	Bone (OxA-21974)		44.9 ± 2.1	44.6–54.9	AMS ^{14}C ultrafiltration	(Wood et al., 2018)
			20	Bone (OxA-10233)		42.1 ± 1.5	42.7–48.7	AMS ^{14}C	(Bernaldo de Quiros et al., 2006)
			20	Bone (OxA-10328)		45.7 ± 1.7	45.4–54.9	AMS ^{14}C	(Bernaldo de Quiros et al., 2006)
			20	Bone (OxA-10327)		>45.7	>45.7	AMS ^{14}C	(Bernaldo de Quiros et al., 2006)
			20	Bone (OxA-10329)		>43.8	>43.8	AMS ^{14}C	(Bernaldo de Quiros et al., 2006)
			20	Bone (OxA-10187)		42.9 ± 1.4	43.2–49.1	AMS ^{14}C	(Bernaldo de Quiros et al., 2006)

(*Continued*)

Table 6. (*Continued*)

Site	Region	Site type	Level (in stratigraphic order; top to bottom)	Material/sample	Age (ka)[a]	Age (^{14}C BP)[b]	Calibrated age range (cal BP)[c]	Method[d]	Reference(s)
			20	Bone (OxA-10188)		>47.3	>43.7	AMS ^{14}C	(Bernaldo de Quiros et al., 2006)
			20c	Bone (OxA-22204)		48.7 ± 3.4	47.0–>55.0	AMS ^{14}C ultrafiltration	(Wood et al., 2018)
			20c	Bone (OxA-22205)		49.4 ± 3.7	47.3–>55.0	AMS ^{14}C ultrafiltration	(Wood et al., 2018)
			20c	Tooth enamel (97131A)	44.7 ± 9.0			ESR/U-series	(Liberda et al., 2010)
			20c	Tooth enamel (97131B)	43.3 ± 9.2			ESR/U-series	(Liberda et al., 2010)
			20c	Tooth enamel (97132B)	45.6 ± 7.9			ESR/U-series	(Liberda et al., 2010)
			20c	Tooth enamel (97133B)	39.6 ± 6.8			ESR/U-series	(Liberda et al., 2010)
			20c	Tooth enamel (97134B)	35.8 ± 6.3			ESR/U-series	(Liberda et al., 2010)
			20c	Tooth enamel (97135A)	46.5 ± 7.9			ESR/U-series	(Liberda et al., 2010)
			20c	Tooth enamel (97136A)	41.7 ± 7.7			ESR/U-series	(Liberda et al., 2010)
			20c	Tooth enamel (97137A)	32.3 ± 5.9			ESR/U-series	(Liberda et al., 2010)
			20c	Tooth enamel (97137A)	39.6 ± 7.9			ESR/U-series	(Liberda et al., 2010)
			20d	Tooth enamel (95480A)	44.2 ± 7.6			ESR/U-series	(Liberda et al., 2010)
			20e	Tooth enamel (CST1A)	47.0 ± 9.4			ESR/U-series	(Liberda et al., 2010)
			20e	Tooth enamel (CST1B)	37.1 ± 5.7			ESR/U-series	(Liberda et al., 2010)
			21	Tooth enamel (90CST3A)	75.5 ± 4.4 (1σ)			ESR/U-series	(Rink et al., 1997)
			21	Tooth enamel (90CST4A)	62.8 ± 4.3 (1σ)			ESR/U-series	(Rink et al., 1997)
			22	Tooth enamel (90CST1A)	80.0 ± 4.4 (1σ)			ESR/U-series	(Rink et al., 1997)
			22	Tooth enamel (90CST1B)	76.7 ± 4.7 (1σ)			ESR/U-series	(Rink et al., 1997)
			22	Tooth enamel (90CST2A)	65.7 ± 4.7 (1σ)			ESR/U-series	(Rink et al., 1997)
			22	Tooth enamel (90CST2B)	59.3 ± 5.0 (1σ)			ESR/U-series	(Rink et al., 1997)
			23c	Travertine	89.0 + 11/–10			U-series	(Bischoff et al., 1992)
El Cuco	Castro-Urdiales, Cantabria	Cave	X	Shell (OxA-27196)		42.4 ± 0.7	44.1–46.4	AMS ^{14}C	(Gutiérrez-Zugasti et al., 2018)
			X	Shell (OxA-27115)		46.2 ± 0.7	46.9–50.8	AMS ^{14}C	(Gutiérrez-Zugasti et al., 2018)
			XII	Shell (Beta-382,681)		>43.5	>43.5	AMS ^{14}C	(Gutiérrez-Zugasti et al., 2018)

(*Continued*)

Table 6. (*Continued*)

Site	Region	Site type	Level (in stratigraphic order; top to bottom)	Material/sample	Age (ka)[a]	Age (^{14}C BP)[b]	Calibrated age range (cal BP)[c]	Method[d]	Reference(s)
			XIII	Shell (OxA-30851)		46.4 ± 0.8	47.0–51.6	AMS ^{14}C	(Gutiérrez-Zugasti et al., 2018)
Cueva Morín	Villanueva de Villaescusa, Cantabria	Cave	11	Charcoal (GifA-96264)		41.8 ± 0.5	43.5–45.6	AMS ^{14}C ABA	(Maíllo-Fernández et al., 2001)
			11	Charcoal (OxA-19459)		43.6 ± 0.6	44.9–47.4	AMS ^{14}C ABOX-SC	(Maroto et al., 2012)
			11	Charcoal (OxA-19083)		41.8 ± 0.5	43.5–45.6	AMS ^{14}C ABA	(Maroto et al., 2012)
La Güelga	Congas de Onis, Asturias	Cave	4b, D exterior	Bone (OxA-20122)		47.4 ± 2.7	46.6–>55.0	AMS ^{14}C ultrafiltration	(Higham et al., 2014)
			4b, D exterior	Bone (OxA-20123)		>43.2	>43.2	AMS ^{14}C ultrafiltration	(Higham et al., 2014)
			4b, D exterior	Bone (OxA-20124)		48.5 ± 3.5	46.8–>55.0	AMS ^{14}C ultrafiltration	(Higham et al., 2014)
			4b, D exterior	Bone (OxA-20125)		>43.6	>43.6	AMS ^{14}C ultrafiltration	(Higham et al., 2014)
			9, D interior	Bone (OxA-19244)		43.7 ± 0.8	44.8–47.9	AMS ^{14}C ultrafiltration	(Higham et al., 2014)
			9, D interior	Bone (OxA-19245)		44.3 ± 1.2	44.7–49.9	AMS ^{14}C ultrafiltration	(Higham et al., 2014)
La Viña	Manzaneda, Asturias	Cave	XIII	Charcoal (OxA-19144)		>59.3	>59.3	AMS ^{14}C ABOX-SC	(Higham et al., 2014)
			XIII	Charcoal (OxA-19196)		>62.0	>62.0	AMS ^{14}C ABA	(Higham et al., 2014)
Sopeña	Avin, Asturias	Cave	XII	Bone (GrA-39761)		35.5 ± 0.7	39.4–41.8	Longin (improved)	(Maroto et al., 2012)
			XII	Tooth (Beta-198146)		38.6 ± 0.8	41.8–43.9	AMS ^{14}C	(Pinto-Llona et al., 2012)
			XII	Bone (GrA-39761)		35.5 ± 0.7	39.4–41.8	AMS ^{14}C	(Pinto-Llona and Grandal d'Anglade, 2019)
			XII	Bone (Beta-470471)		39.4 ± 0.3	42.5–43.1	AMS ^{14}C	(Pinto-Llona and Grandal-d'Anglade, 2019)
			XII	Bone (Beta-470468)		33.1 ± 0.2	37.0–38.7	AMS ^{14}C ultrafiltration	(Pinto-Llona and Grandal-d'Anglade, 2019)
			XII	Bone (Beta-470472)		43.8 ± 0.5	45.2–47.4	AMS ^{14}C	(Pinto-Llona and Grandal-d'Anglade, 2019)
			XII	Bone (Beta-470469)		45.0 ± 0.6	46.0–48.6	AMS ^{14}C ultrafiltration	(Pinto-Llona and Grandal-d'Anglade, 2019)
			XII	Tooth (FT53en1-4)	49.3 ± 5.3			ESR (Linear uptake)	(Pinto-Llona et al., 2012)
			XIII	Tooth (PT7en1)	57.1 ± 12.5			ESR (Linear uptake)	(Pinto-Llona et al., 2012)
			XIV	Tooth (PT9en1)	50.4 ± 8.7			ESR (Linear uptake)	(Pinto-Llona et al., 2012)
			XV	Tooth (PT8en1)	57.2 ± 12.3			ESR (Linear uptake)	(Pinto-Llona et al., 2012)
Adjacent regions									
Arrillor	Zigoitia, Álava	Cave	Lmc	Bone (OxA-21986)		44.9 ± 2.1	44.6–54.9	AMS ^{14}C ultrafiltration	(Iriarte-Chiapusso et al., 2019)
			Lamc A	Bone (OxA-22654)		>46.8	>46.8	AMS ^{14}C ultrafiltration	(Iriarte-Chiapusso et al., 2019)
			Lamc A	Bone (OxA-22655)		45.6 ± 2.3	45.2–>55.0	AMS ^{14}C ultrafiltration	(Iriarte-Chiapusso et al., 2019)

(*Continued*)

Table 6. (*Continued*)

Site	Region	Site type	Level (in stratigraphic order; top to bottom)	Material/sample	Age (ka)[a]	Age (^{14}C BP)[b]	Calibrated age range (cal BP)[c]	Method[d]	Reference(s)
			Amk A	Bone (OxA-22656)		48.5 ± 3.2	47.1–>55.0	AMS ^{14}C ultrafiltration	(Iriarte-Chiapusso et al., 2019)
			Amk A	Bone (OxA-22657)		>45.2	>45.2	AMS ^{14}C ultrafiltration	(Iriarte-Chiapusso et al., 2019)
			Smkl-h B	Bone (OxA-22658)		45.6 ± 2.3	45.2–>55.0	AMS ^{14}C ultrafiltration	(Iriarte-Chiapusso et al., 2019)
Abauntz	Arraitz, Navarre	Cave	h	Bone (GrA-16960)		>45.0	>45.0	AMS ^{14}C	(Utrilla et al., 2015)
			h	Teeth (mean; various samples)	27.5 ± 5.0			ESR	(Utrilla et al., 2015)
			h	Bear teeth	47.0 ± 7.0			AAR	(Utrilla et al., 2015)
Peña Miel	Sierra de Cameros, La Rioja	Cave	c	Bone (OxA-5518)		37.7 ± 1.3	40.5–44.4	AMS ^{14}C	(Montes et al., 2001)
			c	Charcoal (UGRA-128)		39.9 ± 10.5	36.3–>55.0	conv. (?) ^{14}C	(Montes et al., 2001)
			e	Bone (OxA-5519)		40.3 ± 1.6	42.0–47.4	AMS ^{14}C	(Montes et al., 2001)
			e	Bone (GrN-12.123)		45.5 ± 1.3	45.5–52.2	conv. (?) ^{14}C	(Montes et al., 2001)
			g	Bone (CSIC-546)		>40.0	>40.0	conv. (?) ^{14}C	(Montes et al., 2001)
Prado Vargas	Cornejo, Burgos	Cave	N4	Horse tooth	46.4			AAR	(Navazo et al., 2005)
			N4	Charcoal (Beta – 548,572)	48.3 ± 3.2 (1σ)	36.8 ± 0.3	41.2–42.1	AMS ^{14}C ABA	(Ruiz et al., 2021)
			N4	Charcoal (Beta – 548,573)	46.2 ± 3.2 (1σ)	38.9 ± 0.4	42.3–43.0	AMS ^{14}C ABA	(Ruiz et al., 2021)
			N4	Sed. quartz grains (PRA19-1)				Single-grain OSL	(Ruiz et al., 2021)
			N4	Sed. quartz grains (PRA19-2)				Single-grain OSL	(Ruiz et al., 2021)
Cueva Millán	Hortigüela, Burgos	Cave	1a	Charcoal (GrN-11021)		37.6 ± 0.7	41.2–42.7	conv. ^{14}C	(Moure and Garcia Soto, 1982)
			1b	Charcoal (GrN-1161)		37.4 ± 0.6	41.2–42.5	conv. ^{14}C	(Moure and Garcia Soto, 1982)
La Mina	Hortigüela, Burgos	Cave		Tooth (LEB-6012)	52.5			AAR	(Díez et al., 2008)
Cueva Corazon	Mave, Palencia	Cave	2	Burned lithic (MAD-4712BIN)	97 ± 8			TL	(Diez Martín et al., 2011)
			2	Burned lithic (MAD-4715BIN)	96 ± 7			TL	(Diez Martín et al., 2011)
Valdegoba	Huérmeces, Burgos	Cave	7	Capping stalagmitic flowstone	<73.2 ± 5.0			U-series	(Quam et al., 2001)
			5	Bone (OxA-21970)		48.4 ± 3.3	46.7–>55.0	AMS ^{14}C ultrafiltration	(Dalén et al., 2012)
Hotel California	Cardeñuela Riopico, Burgos (Sierra de Atapuerca)	Open-air	V	Sed. quartz grains (HC10-1)	48.2 ± 3.3 (1σ)			Single-grain OSL	(Arnold et al., 2013)
			V	Sed. quartz grains (HC10-4)	48.2 ± 3.9 (1σ)			Single-grain OSL	(Arnold et al., 2013)
			II	Sed. quartz grains (HC10-2)	57.6 ± 5.7 (1σ)			Single-grain OSL	(Arnold et al., 2013)

(*Continued*)

Table 6. (*Continued*)

Site	Region	Site type	Level (in stratigraphic order; top to bottom)	Material/sample	Age (ka)[a]	Age (^{14}C BP)[b]	Calibrated age range (cal BP)[c]	Method[d]	Reference(s)
			I	Sed. quartz grains (HC10-3)	71.0 ± 5.6 (1σ)			Single-grain OSL	(Arnold et al., 2013)
Fuente Mudarra	Cardeñuela Riopico, Burgos (Sierra de Atapuerca)	Open-air	4	Sed. quartz grains (L4 OSL17-01)	56.8 ± 3.3 (1σ)			Multi-grain OSL	(Santamaria et al., 2021)
			5	Sed. quartz grains (L5 OSL17-02)	87.1 ± 5.2 (1σ)			Multi-grain OSL	(Santamaria et al., 2021)
			6	Sed. quartz grains (L6 OSL17-03)	106.7 ± 7.3 (1σ)			Multi-grain OSL	(Santamaria et al., 2021)
			7	Sed. quartz grains (L7 OSL17-04)	118.1 ± 8.7 (1σ)			Multi-grain OSL	(Santamaria et al., 2021)
			8	Sed. quartz grains (L8 OSL17-05)	123.7 ± 8.8 (1σ)			Multi-grain OSL	(Santamaria et al., 2021)
Hundidero	Orbaneja Riopico, Burgos (Sierra de Atapuerca)	Open-air	2	Sed. quartz grains	30.2 ± 3.6 (1σ)			OSL	(Navazo et al., 2011)
			2	Sed. quartz grains	58.8 ± 4.9 (1σ)			TL	(Navazo et al., 2011)
			3	Sed. quartz grains	56.2 ± 4.4 (1σ)			OSL	(Navazo et al., 2011)
			4	Sed. quartz grains	70.6 ± 11 (1σ)			TL	(Navazo et al., 2011)
Galería de las Estatuas	Ibeas de Juarros, Burgos (Sierra de Atapuerca)	Cave	**Pit GE-I**						
			Base	Capping flowstone	14. 2 ± 0.3 (2σ)			U-series	(Martínez-Pillado et al., 2014)
			GE-I, LU1	Bone (Beta - 247621)		>45.0	>45.0	AMS ^{14}C ABA	(Arsuaga et al., 2017)
			GE-I, LU1	Bone (OxA-21523)		43.5 ± 1.8	43.2–52.0	AMS ^{14}C ultrafiltration	(Arsuaga et al., 2017)
			GE-I, LU1	Sed. quartz grains (GE16-2)				Single-grain OSL	(Demuro et al., 2019a)
			GE-I, LU2	Bone (Beta - 247672)	80 ± 5 (1σ)	>45.0	>45.0	AMS ^{14}C ABA	(Arsuaga et al., 2017)
			GE-I, LU2	Bone (OxA-21524)		>45.6	>45.6	AMS ^{14}C ultrafiltration	(Arsuaga et al., 2017)
			GE-I, LU2	Sed. quartz grains (GE16-1)				Single-grain OSL	(Demuro et al., 2019a)
			GE-I, LU2	Tooth (GE1806)	83 ± 5 (1σ)			ESR/U-series	(Moreno et al., 2022)
			GE-I, LU2	Sed. quartz grains (GE16-3)	102 ± 23			Single-grain OSL	(Demuro et al., 2019a)
			GE-I, LU3	Tooth (GE1804)	113 ± 8 (1σ)			ESR/U-series	(Moreno et al., 2022)
			GE-I, LU3	Bone (Beta – 247628)	104 ± 6	>45.0	>45.0	AMS ^{14}C ABA	(Arsuaga et al., 2017)
			GE-I, LU3	Bone (OxA-21525)		44.0 ± 1.9	44.0–54.6	AMS ^{14}C ultrafiltration	(Arsuaga et al., 2017)
			GE-I, LU3	Sed. quartz grains (GE16-4)				Single-grain OSL	(Demuro et al., 2019a)
			GE-I, LU3	Tooth (GE1805)	107 ± 8 (1σ)			ESR/U-series	(Moreno et al., 2022)
			GE-I, LU4	Tooth (GE1803)	179 ± 11			ESR/U-series	(Moreno et al., 2022)
			GE-I, LU4	Sed. quartz grains (GE16-5)	95 ± 33			Single-grain OSL	(Demuro et al., 2019a)
			GE-I, LU4	Tooth (GE1802)	112 ± 7 (1σ)			ESR/U-series	(Moreno et al., 2022)
			GE-I, LU5	Tooth (GE1801)	92 ± 6			ESR/U-series	(Moreno et al., 2022)

(*Continued*)

Table 6. (*Continued*)

Site	Region	Site type	Level (in stratigraphic order; top to bottom)	Material/sample	Age (ka)[a]	Age (^{14}C BP)[b]	Calibrated age range (cal BP)[c]	Method[d]	Reference(s)
			Pit GE-II		276 ± 21				
			Base	Capping flowstone				U-series	(Vernot et al., 2021)
			GE-II, LU1	Bone (OxA-24563)	54 ± 3 (2σ)			AMS ^{14}C ultrafiltration	(Arsuaga et al., 2017)
			GE-II, LU1b	Sed. quartz grains (GE16-6)		44.2 ± 2.0	44.1–54.8	Single-grain OSL	(Demuro et al., 2019a)
			GE-II, LU2	Bone (OxA-24564)	70 ± 5 (1σ)			AMS ^{14}C ultrafiltration	(Arsuaga et al., 2017)
			GE-II, LU2	Sed. quartz grains (GE16-7)		>46.3	>46.3	Single-grain OSL	(Demuro et al., 2019a)
			GE-II, LU2	Tooth (GE1808)	79 ± 5 (1σ)			ESR/U-series	(Moreno et al., 2022)
					115 ± 18				
La Ermita	Hortigüela, Burgos	Cave	Top	Capping flowstone	95 ± 6			U-series	(Sánchez Yustos and Diez Martín, 2015)
			Top	Capping flowstone	102 ± 4			U-series	
			5a	Charcoal (OxA-4603)		31.1 ± 0.6	34.4–36.7	AMS ^{14}C	(Díez et al., 2008)
			5a	Tooth	114 ± 42			AAR	(Díez et al., 2008)
			5a	Tooth	129 ± 39			AAR	(Díez et al., 2008)

[a]Dating uncertainty confidence intervals (1σ or 2σ) are as quoted in the original papers. Where the reported uncertainty confidence interval has not been specified by the authors, we assume that technique-specific reported conventions have been adopted (i.e. OSL, TL and ESR/U-series dating uncertainties = 1σ; U-series and U/Th = 2σ), though we have not designated an uncertainty confidence level to such samples in this table.
[b]Uncalibrated ^{14}C age uncertainties presented at 1σ.
[c]Calibrated age presented at 95.4% probability range. ^{14}C dates were calibrated using OxCal 4.4 (Ramsey, 2009) and IntCal20 (Reimer et al., 2020).
[d]AAR = amino acid racemization; AMS ^{14}C = accelerator mass spectrometry ^{14}C; AMS ^{14}C ABA = acid–base–acid treatment; AMS ^{14}C ABOX-SC = acid and base treatment, followed by an oxidation stage and pre-combustion; conv. ^{14}C = conventional ^{14}C; ESR = electron spin resonance; OSL = optically stimulated luminescence; TT-OSL = thermally transferred OSL; TL = thermoluminescence.

ecological turnover taking place at Axlor between the end of the last interglacial complex and the onset of MIS 4, a change that appears to reflect orbitally driven climatic deterioration, rather than local-scale environmental changes occurring at this time.

Apart from the data on the large mammal assemblages, more precise palaeoenvironmental information for levels M, F and B is currently lacking, as palynological, micromorphological and biomarker analyses are still in progress.

Regional cultural interpretations

The new chronology for Axlor indicates that the lower levels containing Levallois knapping products (level N) accumulated ~100–90 ka (MIS 5), while the upper level characterized by Quina elements (level D) accumulated ~70 ka (late MIS 5 to early MIS 4; Table 5). This study provides the first such long-range, ordered and well-dated Middle Palaeolithic succession in the north Atlantic Iberian region, with most neighbouring sites still poorly dated (Table 6; cf. Deschamps, 2019). The lack of a firmly established chronological framework for this region has previously hampered attempts to explore Middle Palaeolithic evolutionary trends and dynamics of cultural change. However, in nearby southwestern France, a much clearer pattern of change had been proposed between the different cultural techno-complexes dating from MIS 5 to MIS 3 (Delagnes and Meignen, 2006; Delagnes and Rendu, 2011; Discamps et al., 2011; Discamps and Royer, 2017; Jaubert, 2012). These models proposed an ordered succession of Levallois, followed by Quina and then by various technical strategies (discoidal with denticulate or MTA – Mousterian in the Acheulean tradition), with each cultural phase being almost coincident with the succession of isotopic stages (MIS 5/4/3). These models relied extensively on stratigraphic and faunal associations to infer climatic periods and hence chronologies. However, new evidence provided by numerical dating studies of several sites across southern France reveals a more complex picture (Richter et al., 2013a; Jacobs et al., 2016; Talamo et al., 2020; Frouin et al., 2017a; 2017b; Guérin et al., 2015b; 2017). This includes the possibility that the Quina complex appeared earlier than originally thought, within MIS 5, and that technical features originally attributed to specific phases (e.g. Levallois knapping or biface production) may be documented across multiple phases, or may appear across almost the entire period.

Parts of the southwest France cultural change 'model' fit the evidence observed at several Middle Palaeolithic sites from northern Iberia, though broad-scale temporal correlations of technical development are much more difficult to establish in this region (Figures 1 and 9; Table 6). At Arrillor (Álava), which is located on the northern flank of the Ebro basin (<20 km from Axlor), the Middle Palaeolithic sequence exhibits long-term technological development (Iriarte-Chiapusso et al., 2019), starting with Levallois in the middle units (level Smk-l), followed by a denticulate Mousterian industry in the overlying units (levels Smc and Smb), and finally Late Mousterian assemblages in upper levels (Lamc and Lmc) (Iriarte-Chiapusso et al., 2019). At Lezetxiki I (Gipuzkoa), also located near Axlor, the extensive excavated sedimentary sequence contains a series of archaeological layers with Levallois technology in the lower part (levels VI, V and IV). Quina presence in level III is difficult to evaluate given the mixed nature (with Middle and Upper Palaeolithic tools) of the assemblage. However, it is not yet possible to determine if these technological replacements are coeval across this region because of the limited chronological control available for the relevant levels at these sites (Álvarez-Alonso and Arrizabalaga, 2012; Falguères, 2005; Iriarte-Chiapusso et al., 2019; Lazuén and Altuna, 2012) (Table 6). Further afield at the site of El Esquilleu, Cantabria province (~200 km west of Axlor), discoid-dominant methods appear both at the top and base of the sequence, while several alternating Quina- and Levallois-dominated levels are found interstratified in the sequence (Cuartero et al., 2015). The Quina industry in levels 11–15 has been ^{14}C dated to 40–43 ka (Table 6), but this is based on two charcoal samples prepared with standard pre-treatment (Baena et al., 2012; Cuartero et al., 2015). These Quina layers are in turn underlain by levels 17–22, which exhibit a complex mix of stratigraphically inverted and infinite ^{14}C ages and two tentative TL ages of 51–53.5 ka (Ascough et al., 2010; Baena et al., 2012; Bird et al., 2010; Jordá Pardo et al., 2008); however, both of these TL ages have been published without methodological details so it is difficult to ascertain their reliability. Due to the limited sample coverage at this site, and apparent ^{14}C complexities affecting many of the Middle Palaeolithic levels, we consider that further dating is needed at El Esquilleu to determine its temporal relationship with Axlor. Finally, at the site of Covalejos (Cantabria province), the Middle Palaeolithic sequence preserves Levallois layers overlain by Quina layers. Though chronological constraints are limited at this site, the richest archaeological layers (levels 6–9) have been constrained to between ~92 and ~40 ka based on U–Th dating of a basal stalagmitic crust, single-grain OSL dating of sedimentary quartz grains, TL dating of a hearth and ^{14}C dating (Sanguino and Montes, 2005; Guérin and Lahaye, 2022). These layers are potentially correlative with the level B–N sequence at Axlor, though this assertion would require further chronological constraints as some of the age control for Covalejos is lacking sufficient methodological information to enable meaningful evaluations of dating reliability.

The new dating results for Axlor help to clarify the technological replacement process in northern Iberia, and provide an important chronological reference for the region. Level N of Axlor documents clear Levallois systems, microflake production and the use of projectile points (González-Urquijo, 2005, 2006) associated with characteristic northern Iberian palaeoenvironmental conditions during MIS 5 (mountainous, temperate and forest-covered setting). The new chronology for level D indicates the presence of a well-developed Quina system around the MIS 5/MIS 4 transition, which was devoted to the production of thick scrapers (>50% of the tools) with ramificated management of resharpening flakes, generalized long-distance transport of lithic raw materials and exploitation of large herbivores (bison and horses) (González-Urquijo, 2005, 2006; González-Urquijo et al., 2014). The new chronological framework for level D is consistent with those from other Quina sites in France and Italy (Jéquier et al., 2015; Richter et al., 2013b; Slimak et al., 2022), and points to an older and more complex (i.e. multiregional) model for the origin of the Quina techno-complex.

Conclusion

This study presents the first chronological constraints for Axlor levels N–B, which represents one of the most characteristic Middle Palaeolithic sequences of the North Atlantic Iberian region. Single-grain OSL dating of sedimentary quartz grains from levels N, M and F produce ages of 99.6 ± 7.6, 89.0 ± 6.5 and 80.0 ± 5.8 ka, respectively, indicating that the lower part of the sequence formed during MIS 5 (probably MIS 5d–a). The overlying levels D and B are OSL dated to 70.4 ± 5.3 and 50.7 ± 3.5 ka, respectively, and were deposited from the MIS 5/MIS 4 transition until early to mid-MIS 3. A replicate single-grain TT-OSL age of 95.6 ± 8.7 ka obtained for the lowermost

sample in level N supports the OSL dating results, reinforcing the newly established MIS 5–MIS 3 chronological framework for this Middle Palaeolithic sequence.

Our new chronology reveals that Axlor does not represent one of the latest Neanderthal occupations of the region, as potentially inferred from the minimum ^{14}C ages obtained for the upper levels. Instead, the site documents a long-range Middle Palaeolithic sequence spanning 50 kyr, and covering several marine isotope stages. The OSL dating results presented here thus reinforce recent findings at Iberian sites such as Galería de las Estatuas, Gruta da Oliveira and Figuera Brava, which underline the need to independently date Middle Palaeolithic records using alternative techniques that are capable of surpassing the ^{14}C upper age limit. The technological change observed at Axlor, whereby Levallois occurring at 105–95 ka (when considering the 1σ error ranges) is replaced by Quina at 75–65 ka, is broadly coeval with trends observed in southwest France and Italy. This technological replacement could potentially be correlated with similar events recorded in other Middle Palaeolithic sequences from the North Atlantic Iberian region, though further chronological work is required at these other sites to ascertain regional trends more definitively.

Supporting information

Additional supporting information may be found in the online version of this article at the publisher's web-site.

Acknowledgements. Research at the Axlor site is funded by the Spanish Ministry of Science and Innovation (Project PID2019-107260GB-I00) and Bizkaiko Foru Aldundia. M.D. was supported by Australian Research Council (ARC) Future Fellowship FT200100816 and ARC Discovery Early Career Researcher Award DE160100743. T.L. is a postdoctoral researcher in the María Zambrano Programme for the attraction of international talent. (NextGenerationEU).

Data availability statement

The data that support the findings of this study are available from the corresponding author upon reasonable request.

Abbreviations. ABOx-SC, acid base oxidation-stepped combustion; ADM, average dose model; CAM, central age model; D_e, equivalent dose; ESR, electron spin resonance; et al., et alii (meaning *and others*); HRGS, high-resolution gamma-ray spectrometry; IR, infrared; LED, light-emitting diode; L_{max}, maximum log likelihood; LST, lithium heteropolytungstate; MAM, minimum age models; MIS, Marine Isotope Stage; OSL, optically stimulated luminescence; SAR, single-aliquot regenerative; TL, thermoluminescence; T_n, natural test dose signal; TT-OSL, thermally transferred optically stimulated luminescence.

References

Aitken, M.J. (1985) *Thermoluminescence dating*. London: Academic Press.

Aitken, M.J. (1998) *An introduction to optical dating: the dating of Quaternary sediments by the use of photon-stimulated luminescence*. Oxford: Oxford University Press.

Allkofer, O. (1974) Introduction to Cosmic Radiation Verlag Karl Thiemig, Munich.

Álvarez-Alonso, D. & Arrizabalaga, A. (2012) Lower stratigraphical sequence of Lezetxiki cave (Arrasate, Basque Country). A necessary reflection. *Zephyrus*, 69, 15–39.

Arnold, L.J., Bailey, R.M. & Tucker, G.E. (2007) Statistical treatment of fluvial dose distributions from southern Colorado arroyo deposits. *Quaternary Geochronology*, 2, 162–167.

Arnold, L.J., Demuro, M., Navazo, M., Benito-Calvo, A. & Pérez-González, A. (2013) OSL dating of the Middle Palaeolithic Hotel California site, Sierra de Atapuerca, north-central Spain. *Boreas*, 42, 285–305.

Arnold, L.J., Demuro, M., Parés, J.M., Arsuaga, J.L., Aranburu, A., Bermúdez de Castro, J.M. et al. (2014) Luminescence dating and palaeomagnetic age constraint on hominins from Sima de los Huesos, Atapuerca, Spain. *Journal of Human Evolution*, 67, 85–107.

Arnold, L.J., Demuro, M., Parés, J.M., Pérez-González, A., Arsuaga, J.L., Bermúdez de Castro, J.M. et al. (2015) Evaluating the suitability of extended-range luminescence dating techniques over early and Middle Pleistocene timescales: published datasets and case studies from Atapuerca, Spain. *Quaternary International*, 389, 167–190.

Arnold, L.J., Demuro, M. & Ruiz, M.N. (2012a) Empirical insights into multi-grain averaging effects from 'pseudo' single-grain OSL measurements. *Radiation Measurements*, 47, 652–658.

Arnold, L.J., Demuro, M., Spooner, N.A., Prideaux, G.J., McDowell, M.C., Camens, A.B. et al. (2019) Single-grain TT-OSL bleaching characteristics: Insights from modern analogues and OSL dating comparisons. *Quaternary Geochronology*, 49, 45–51.

Arnold, L.J., Duval, M., Demuro, M., Spooner, N.A., Santonja, M. & Pérez-González, A. (2016) OSL dating of individual quartz 'super-grains' from the Ancient Middle Palaeolithic site of Cuesta de la Bajada, Spain. *Quaternary Geochronology*, 36, 78–101.

Arnold, L.J., Duval, M., Falguères, C., Bahain, J.J. & Demuro, M. (2012b) Portable gamma spectrometry with cerium-doped lanthanum bromide scintillators: suitability assessments for luminescence and electron spin resonance dating applications. *Radiation Measurements*, 47, 6–18.

Arnold, L.J. & Roberts, R.G. (2009) Stochastic modelling of multi-grain equivalent dose (De) distributions: Implications for OSL dating of sediment mixtures. *Quaternary Geochronology*, 4, 204–230.

Arnold, L.J. & Roberts, R.G. (2011) Paper I - Optically stimulated luminescence (OSL) dating of perennially frozen deposits in north-central Siberia: OSL characteristics of quartz grains and methodological considerations regarding their suitability for dating: Optically stimulated luminescence (OSL) dating of perennially frozen deposits in north-central Siberia. *Boreas*, 40, 389–416.

Arnold, L.J., Roberts, R.G., Galbraith, R.F. & DeLong, S.B. (2009) A revised burial dose estimation procedure for optical dating of youngand modern-age sediments. *Quaternary Geochronology*, 4, 306–325.

Arnold, L.J., Roberts, R.G., Macphee, R.D.E., Haile, J.S., Brock, F., Möller, P. et al. (2011) Paper II - Dirt, dates and DNA: OSL and radiocarbon chronologies of perennially frozen sediments in Siberia, and their implications for sedimentary ancient DNA studies. *Boreas*, 40, 417–445.

Arnold, L.J., Roberts, R.G., MacPhee, R.D.E., Willerslev, E., Tikhonov, A.N. & Brock, F. (2008) Optical dating of perennially frozen deposits associated with preserved ancient plant and animal DNA in north-central Siberia. *Quaternary Geochronology*, 3, 114–136.

Arsuaga, J.L., Gómez-Olivencia, A., Sala, N., Martínez-Pillado, V., Pablos, A., Bonmatí, A. et al. (2017) Evidence of paleoecological changes and Mousterian occupations at the Galería de las Estatuas site, Sierra de Atapuerca, northern Iberian plateau, Spain. *Quaternary Research*, 88, 345–367.

Ascough, P.L., Bird, M.I., Meredith, W., Wood, R.E., Snape, C.E., Brock, F. et al. (2010) Hydropyrolysis: Implications for radiocarbon pretreatment and characterization of black carbon. *Radiocarbon*, 52, 1336–1350.

Bachellerie, F. (2011) Quelle unité pour le Châtelperronien? Apport de l'analyse taphonomique et techno-économique des industries lithiques de trois gisements aquitains de plein air: le Basté, Bidart (Pyrénées-Atlantiques) et Canaule II (Dordogne). PhD thesis, (2011).

Baena, J., Carrión, E., Cuartero, F. & Fluck, H. (2012) A chronicle of crisis: the Late Mousterian in north Iberia (Cueva del Esquilleu, Cantabria, Spain). *Quaternary International*, 247, 199–211.

Baena, J., Elena Carrion, E., Ruiz, B., Ellwood, B., Sese, C., Yravedra, J. et al. (2005) Paleoecología y comportamiento humano durante el Pleistoceno Superior en la comarca de Liébana: La secuencia de la Cueva de El Esquilleu (Occidente de Cantabria, España), In: Montes, R. & Lasheras, J.A. (Eds.), Actas de La Reunión Científica: Neandertales Cantábricos, estado de la cuestión. Museo Nacional y Centro de Investigación de Altamira, pp. 461–487.

Bailey, R.M. & Arnold, L.J. (2006) Statistical modelling of single grain quartz D_e distributions and an assessment of procedures for estimating burial dose. *Quaternary Science Reviews*, 25, 2475–2502.

Barandiarán, J.M. (1980) Excavaciones en Axlor. Obras completas La Gran Enciclopedia Vasca, vol. XVII.

Benito-Calvo, A., Arnold, L.J., Mora, R., Martínez-Moreno, J. & Demuro, M. (2020) Reconstructing Mousterian landscapes in the southeastern Pyrenees (Roca dels Bous site, Pre-Pyrenees ranges, Spain). *Quaternary Research*, 97, 167–186.

Bernaldo de Quiros, F., Cabrera Valdes, V. & Stuart, A.J. (2006) Nuevas dataciones para el Musteriense y el Magdaleniense de la Cueva de el Castillo, in: Valdes, V., Bernaldo de Quiros, F., & Maíllo-Fernandez, J.M. (Eds.), En el centenario de la cueva de El Castillo: El ocaso de los Neandertales. Centro Asociado a la Universidad Nacional de Educacion a Distancia en Cantabria, Madrid, pp. 455-457.

Bird, M.I., Charville-Mort, P.D.J., Ascough, P.L., Wood, R., Higham, T. & Apperley, D. (2010) Assessment of oxygen plasma ashing as a pre-treatment for radiocarbon dating. *Quaternary Geochronology*, 5, 435–442.

Bischoff, J.L., Garcia, J.F. & Straus, L.G. (1992) Uranium-series isochron dating at El Castillo cave (Cantabria, Spain): the "Acheulean"/"Mousterian" question. *Journal of Archaeological Science*, 19, 49–62.

Bøtter-Jensen, L. & Mejdahl, V. (1988) Assessment of beta dose-rate using a GM multicounter system. International Journal of Radiation Applications and Instrumentation. *Part*, 14, 187–191.

Bowler, J.M., Johnston, H., Olley, J.M., Prescott, J.R., Roberts, R.G., Shawcross, W. et al. (2003) New ages for human occupation and climatic change at Lake Mungo, Australia. *Nature*, 421, 837–840.

Brennan, B.J. (2003) Beta doses to spherical grains. *Radiation Measurements*, 37, 299–303.

Bronk Ramsey, C. (2009) Bayesian analysis of radiocarbon dates. *Radiocarbon*, 51, 337–360.

Cabanes, D., Mallol, C., Expósito, I. & Baena, J. (2010) Phytolith evidence for hearths and beds in the late Mousterian occupations of Esquilleu cave (Cantabria, Spain). *Journal of Archaeological Science*, 37, 2947–2957.

Castaños, P. (2005) Revisión actualizada de las faunas de macromamíferos del Würm antiguo en la Región Cantábrica. In: Montes, R. & Lasheras, J.A. (Eds.), Actas de La Reunión Científica: Neandertales Cantábricos, estado de la cuestión. Museo Nacional y Centro de Investigación de Altamira, pp. 201-207.

Cuartero, F., Alcaraz-Castaño, M., López-Recio, M., Carrión-Santafé, E. & Baena-Preysler, J. (2015) Recycling economy in the mousterian of the Iberian Peninsula: the case study of El Esquilleu. *Quaternary International*, 361, 113–130.

Dalen, L., Orlando, L., Shapiro, B., Brandstrom-Durling, M., Quam, R., Gilbert, M.T.P. et al. (2012) Partial genetic turnover in neandertals: continuity in the east and population replacement in the West. *Molecular Biology and Evolution*, 29, 1893–1897.

Daniau, A.L., Goñi, M.F.S. & Duprat, J. (2009) Last glacial fire regime variability in western France inferred from microcharcoal preserved in core MD04-2845, Bay of Biscay. *Quaternary Research*, 71, 385–396.

Daura, J., Sanz, M., Demuro, M., Arnold, L.J., Costa, A.M., Moreno, J. et al. (2021) A new chronological framework and site formation history for Cova del Gegant (Barcelona): Implications for Neanderthal and Anatomically Modern Human occupation of NE Iberian Peninsula. *Quaternary Science Reviews*, 270, 107141. Available from: https://doi.org/10.1016/j.quascirev.2021.107141

Delagnes, A. & Meignen, L. (2006) Diversity of Lithic Production Systems During the Middle Paleolithic in France Are There Any Chronological Trends? In: Hovers, E. & Kuhn, S. (Eds.) *Transitions before the Transition: Evolution and Stability in the Middle Paleolithic and Middle Stone Age*. Springer. pp. 85–107.

Delagnes, A. & Rendu, W. (2011) Shifts in Neandertal mobility, technology and subsistence strategies in western France. *Journal of Archaeological Science*, 38, 1771–1783.

Demuro, M., Arnold, L.J., Aranburu, A., Gómez-Olivencia, A. & Arsuaga, J.L. (2019a) Single-grain OSL dating of the Middle Palaeolithic site of Galería de las Estatuas, Atapuerca (Burgos, Spain). *Quaternary Geochronology*, 49, 254–261.

Demuro, M., Arnold, L.J., Aranburu, A., Sala, N. & Arsuaga, J.L. (2019b) New bracketing luminescence ages constrain the Sima de los Huesos hominin fossils (Atapuerca, Spain) to MIS 12. *Journal of Human Evolution*, 131, 76–95.

Demuro, M., Arnold, L.J., Duval, M., Méndez-Quintas, E., Santonja, M. & Pérez-González, A. (2020) Refining the chronology of Acheulean deposits at Porto Maior in the River Miño basin (Galicia, Spain) using a comparative luminescence and ESR dating approach. *Quaternary International*, 556, 96–112.

Demuro, M., Arnold, L.J., Froese, D.G. & Roberts, R.G. (2013) OSL dating of loess deposits bracketing Sheep Creek tephra beds, northwest Canada: dim and problematic single-grain OSL characteristics and their effect on multi-grain age estimates. *Quaternary Geochronology*, 15, 67–87.

Demuro, M., Arnold, L.J., Parés, J.M., Pérez-González, A., Ortega, A.I., Arsuaga, J.L. et al. (2014) New luminescence ages for the Galería Complex archaeological site: Resolving chronological uncertainties on the Acheulean record of the Sierra de Atapuerca, Northern Spain. *PLoS One*, 9(10), e110169.

Demuro, M., Arnold, L.J., Parés, J.M. & Sala, R. (2015) Extended-range luminescence chronologies suggest potentially complex bone accumulation histories at the Early-to-Middle Pleistocene palaeontological site of Huéscar-1 (Guadix-Baza basin, Spain). *Quaternary International*, 389, 191–212.

Demuro, M., Roberts, R.G., Froese, D.G., Arnold, L.J., Brock, F. & Ramsey, C.B. (2008) Optically stimulated luminescence dating of single and multiple grains of quartz from perennially frozen loess in western Yukon Territory, Canada: Comparison with radiocarbon chronologies for the late Pleistocene Dawson tephra. *Quaternary Geochronology*, 3, 346–364.

Deschamps, M. (2017) Late Middle Palaeolithic assemblages with flake cleavers in the western Pyrenees: the Vasconian reconsidered. *Quaternary International*, 433, 33–49.

Deschamps, M. (2019) Identification of Quina and Vasconian technocomplexes in Gatzarria Cave (north-western Pyrenees), based on the stratigraphic, taphonomic and technological revision of the Georges Laplace collections. *Comptes Rendus Palevol*, 18, 569–586.

Devièse, T., Abrams, G., Hajdinjak, M., Pirson, S., de Groote, I., Modica, K.D. et al. (2021) Reevaluating the timing of Neanderthal disappearance in Northwest Europe. Proceedings of the National Academy of Sciences of the United States of America 118 No. 12 e2022466118.

Díez, C., Alonso, R., Bengoechea, A., Colina, A., Jordá, J.F., Navazo, M. et al. (2008) El Paleolítico Medio en el valle del Arlanza (Burgos), los sitios de La Ermita, Millán y La Mina. *Quaternario y Geomorfolgía*, 22, 135–157.

Diez Martín, F., Sánchez Yustos, P., Gómez González, J.A., Gómez de la Rua, D., Yravedra Sáinz de los Terreros, J. & Díaz Muñoz, I. (2011) La ocupacion neandertal en el Cañon de La Horadada (Mave, Palencia, España): nuevas perspectivas arqueológicas en Cueva Corazón. *Munibe*, 62, 65–85.

Discamps, E., Jaubert, J. & Bachellerie, F. (2011) Human choices and environmental constraints: Deciphering the variability of large game procurement from Mousterian to Aurignacian times (MIS 5-3) in southwestern France. *Quaternary Science Reviews*, 30, 2755–2775.

Discamps, E. & Royer, A. (2017) Reconstructing palaeoenvironmental conditions faced by Mousterian hunters during MIS 5 to 3 in southwestern France: A multi-scale approach using data from large and small mammal communities. *Quaternary International*, 433, 64–87.

Doerschner, N., Fitzsimmons, K.E., Blasco, R., Finlayson, G., Rodríguez-Vidal, J., Rosell, J. et al. (2019) Chronology of the Late Pleistocene archaeological sequence at Vanguard Cave, Gibraltar: Insights from quartz single and multiple grain luminescence dating. *Quaternary International*, 501, 289–302.

Duller, G.A.T. (2003) Distinguishing quartz and feldspar in single grain luminescence measurements. *Radiation Measurements*, 37, 161–165.

Duller, G.A.T. (2007) Assessing the error on equivalent dose estimates derived from single aliquot regenerative dose measurements. *Ancient TL*, 25, 15–24.

Duval, M. & Arnold, L.J. (2013) Field gamma dose-rate assessment in natural sedimentary contexts using LaBr3(Ce) and NaI(Tl) probes: A comparison between the "threshold" and "windows" techniques. *Applied Radiation and Isotopes*, 74, 36–45.

Falguères, C., Yokoyama, Y. & Arrizabalaga, A. (2005) La geocronología del yacimiento pleistocénico de Lezetxiki (Arrasate, País Vasco). Crítica de las dataciones existentes y algunas nuevas aportaciones. *Munibe Antropologia-Arkeologia*, 57, 93–106.

Frías, D. (2013) Nuevas aportaciones al estudio del Musteriense final cantábrico: el utillaje lítico del nivel D de Axlor (Dima, Vizcaya). MA thesis. Universidad de Cantabria.

Frouin, M., Lahaye, C., Mercier, N., Guibert, P., Couchoud, I., Texier, J.P. et al. (2017a) Chronologie du site moustérien de type Quina des Pradelles (Marillac-le-Franc, Charente, France). *PALEO. Revue d'archéologie préhistorique*, 28, 117–136.

Frouin, M., Lahaye, C., Valladas, H., Higham, T., Debénath, A., Delagnes, A. et al. (2017b) Dating the middle Paleolithic deposits of La Quina Amont (Charente, France) using luminescence methods. *Journal of Human Evolution*, 109, 30–45.

Galbraith, R. (2002) A note on the variance of a background-corrected OSL count. *Ancient TL*, 20, 49–51.

Galbraith, R.F., Roberts, R.G., Laslett, G.M., Yoshida, H. & Olley, J.M. (1999) Optical dating of single and multiple grains of quartz from Jinmium rock shelter, northern Australia: Part I, experimental design and statistical models. *Archaeometry*, 41, 339–364.

Garcia-Ibaibarriaga, N., Rofes, J., Bailon, S., Garate, D., Rios-Garaizar, J., Martínez-García, B. et al. (2015) A palaeoenvironmental estimate in Askondo (Bizkaia, Spain) using small vertebrates. *Quaternary International*, 364, 244–254.

Gómez-Orellana, L., Ramil-Rego, P. & Muñoz Sobrino, C. (2007) The Würm in NW Iberia, a pollen record from Area Longa (Galicia). *Quaternary Research*, 67, 438–452.

González-Urquijo, J. (2009) Axlor. *Arkeoikuska*, 8, 245–248.

González-Urquijo, J., Ibáñez, J.J., Ríos, J. & Bourguignon, L. (2006) Aportes de las nuevas excavaciones en Axlor sobre el final del Paleolítico Medio. In: Cabrera, V.B.d.Q., Maíllo, F., & J.M. (Eds.) *En el centenario de la cueva de El Castillo: el ocaso de los neandertales*. Madrid: UNED. pp. 269–290.

González-Urquijo, J., Ibáñez, J.J., Ríos, J., Bourguignon, L., Castaños, P. & Tarriño, A. (2005) Excavaciones recientes en Axlor. Movilidad y planificación de actividades en grupos de neandertales. In: Montes, R. & Lasheras, J.A. (Eds.), Actas de La Reunión Científica: Neandertales Cantábricos. Estado de la Cuestión. Museo Nacional y Centro de Investigación de Altamira, pp. 527-539.

González-Urquijo, J., I., J.J., Lazuén, T. & Mozota, M. (2014) Axlor. In Los cazadores recolectores del Pleistoceno y del Holoceno en Iberia y el Estrecho de Gibraltar: estado actual del conocimiento del registro arqueológico, Sala, R. (Ed.). Universidad de Burgos/Museo de Evolución Humana, pp. 11–14.

González-Urquijo, J., Bailey, S.E. & Lazuen, T. (2021) Axlor's level IV human remains are convincingly Neanderthals: a reply to Gómez-Olivencia et al. *American Journal of Physical Anthropology*, 176, 553–558.

Gonzalez Echegaray, J. & Freeman, L.G. (1971) Cueva Morín: Excavaciones 1966–1968. Patronato de Cuevas Prehistóricas.

Guérin, G., Frouin, M., Talamo, S., Aldeias, V., Bruxelles, L., Chiotti, L. et al. (2015b) A multi-method luminescence dating of the Palaeolithic sequence of La Ferrassie based on new excavations adjacent to the La Ferrassie 1 and 2 skeletons. *Journal of Archaeological Science*, 58, 147–166.

Guérin, G., Frouin, M., Tuquoi, J., Thomsen, K.J., Goldberg, P., Aldeias, V. et al. (2017) The complementarity of luminescence dating methods illustrated on the Mousterian sequence of the Roc de Marsal: A series of reindeer-dominated, Quina Mousterian layers dated to MIS 3. *Quaternary International*, 433, 102–115.

Guérin, G., Jain, M., Thomsen, K.J., Murray, A.S. & Mercier, N. (2015a) Modelling dose rate to single grains of quartz in well-sorted sand samples: the dispersion arising from the presence of potassium feldspars and implications for single grain OSL dating. *Quaternary Geochronology*, 27, 52–65.

Guérin, G. & Lahaye, C. (2022) Luminiscence dating at Cueva de Covalejos (Cantabria, Spain): preliminary results. Ramón Montes Barquín; Juan Sanguino González. La Cueva de Covalejos (Velo de Piélagos, Cantabria): Ocupaciones neandertales y sapiens en la cuenca baja del río Pas: actuaciones arqueológicas 1997-1999 y 2002, Museo de Prehistoria y Arqueología de Cantabria, 2021. Gutiérrez-Zugasti, I., Rios-Garaizar, J., Marín-Arroyo, A.B., Rasines del Río, P., Maroto, J., Jones, J.R., Bailey, G.N., Richards, M.P. (2018) A chrono-cultural reassessment of the levels VI–XIV from El Cuco rock-shelter: a new sequence for the Late Middle Paleolithic in the Cantabrian region (northern Iberia). *Quaternary International*, 474, 44–55.

Guérin, G., Mercier, M. & Adamiec, G. (2011) Dose-rate conversion factors: update. *Ancient TL*, 29, 5–8.

Higham, T., Douka, K., Wood, R., Ramsey, C.B., Brock, F., Basell, L. et al. (2014) The timing and spatiotemporal patterning of Neanderthal disappearance. *Nature*, 512, 306–309.

Hoffmann, D.L., Standish, C.D., García-Diez, M., Pettitt, P.B., Milton, J.A., Zilhão, J. et al. (2018) U-Th dating of carbonate crusts reveals Neandertal origin of Iberian cave art. *Science*, 359, 912–915.

Hublin, J.J. (2017) The last Neanderthal. *Proceedings of the National Academy of Sciences*, 114, 10520–10522.

Iriarte-Chiapusso, M.J., Wood, R. & Sáenz de Buruaga, A. (2019) Arrillor cave (Basque Country, northern Iberian Penisula). Chronological, palaeo-environmental and cultural notes on a long Mousterian sequence. *Quaternary International*, 508, 107–115.

Jacobs, Z., Duller, G.A.T., Wintle, A.G. & Henshilwood, C.S. (2006) Extending the chronology of deposits at Blombos Cave, South Africa, back to 140 ka using optical dating of single and multiple grains of quartz. *Journal of Human Evolution*, 51, 255–273.

Jacobs, Z., Jankowski, N.R., Dibble, H.L., Goldberg, P., McPherron, S.J.P., Sandgathe, D. et al. (2016) The age of three Middle Palaeolithic sites: single-grain optically stimulated luminescence chronologies for Pech de l'Azé I, II and IV in France. *Journal of Human Evolution*, 95, 80–103.

Jankowski, N.R., Stern, N., Lachlan, T.J. & Jacobs, Z. (2020). A high-resolution late Quaternary depositional history and chronology for the southern portion of theLake Mungo lunette, semi-arid Australia. Quaternary Science Reviews 233, 106224.

Jaubert, J. (2012) Les archéo-sequences du Paléolithique moyen du Sud-Ouest de la France: what does a quarte de siècle après François Bordes? In: Delpech, F. & Jaubert, J. (Eds.) *François Bordes et la Préhistoire*. CTHS: Actes du colloque international François Bordes. pp. 235–253.

Jéquier, C., Peresani, M., Romandini, M., Delpiano, D., Joannes-Boyau, R., Lembo, G. et al. (2015) The De Nadale Cave, a single layered Quina Mousterian site in the North of Italy. *Quartar*, 62, 7–21.

Jordá Pardo, J.F., Baena Preysler, J., Carral González, P., Garcia-Guinea, J., Correcher Delgado, V. & Yravedra Sainz de los Terreros, J. (2008) Sedimentary and diagenetic processes in the archaelogical record from Pleistocene site of El Esquilleu cave (Los Picos de Europa, North of Spain). *Cuaternario y Geomorfologia*, 22, 31–46.

Karkanas, P. & Goldberg, P. (2019) *Reconstructing Archaeological Sites: Understanding the Geoarchaeological Matrix*. John Wiley & Sons.

Lalueza-Fox, C., Rosas, A., Estalrrich, A., Gigli, E., Campos, P.F., García-Tabernero, A. et al. (2011) Genetic evidence for patrilocal mating behavior among Neandertal groups. *Proceedings of the National Academy of Sciences*, 108, 250–253.

Lambrecht, G., Rodríguez de Vera, C., Jambrina-Enríquez, M., Crevecoeur, I., Gonzalez-Urquijo, J., Lazuen, T. et al. (2021) Characterisation of charred organic matter in micromorphological thin sections by means of Raman spectroscopy. Archaeological and Anthropological Sciences 13. *Article number*, 13. https://doi.org/10.1007/s12520-020-01263-3

Lazuen, T. (2012) European Neanderthal stone hunting weapons reveal complex behaviour long before the appearance of modern humans. *Journal of Archaeological Science*, 39, 2304–2311.

Lazuen, T. & Altuna, J. (2012) Technological organization of the first Neanderthal societies in the Cantabrian region. *Interpreting the lithic industry and fauna from the lowermost levels (V, VI and VII) of Lezetxiki cave. Zephyrus*, 69, 41–74.

Lazuen, T. & González-Urquijo, J. (2015) Recycling in the early middle paleolithic: The role of resharpening flakes assessed through techno-functional analysis. *Quaternary International*, 361, 229–237.
Lazuen, T. & González Urquijo, J. (2020) El estudio de las formas de vida de las sociedades neandertales en el yacimiento de Axlor: las excavaciones de J.M. Barandiaran y el proyecto del siglo XXI. Anuario de Eusko. *Folklore*, 54, 47–69.
Lewis, R.J., Tibby, J., Arnold, L.J., Barr, C., Marshall, J., McGregor, G. et al. (2020) Insights into subtropical Australian aridity from Welsby Lagoon, north Stradbroke Island, over the past 80,000 years. *Quaternary Science Reviews*, 234, 106262.
Liberda, J.J., Thompson, J.W., Rink, J., Bernaldo de Quirós, F., Jayaraman, R., Selvaretinam, K. et al. (2010) ESR Dating of Tooth Enamel in Mousterian Layer 20, El Castillo, Spain. *Geoarchaeology: An International Journal*, 25, 467–474.
Lisiecki, L.E. & Raymo, M.E. (2005) A Pliocene-Pleistocene stack of 57 globally distributed benthic δ 18O records. *Paleoceanography*, 20, 1–17.
Lisiecki, L.E. & Stern, J.V. (2016) Regional and global benthic δ18O stacks for the last glacial cycle. *Paleoceanography*, 31, 1368–1394.
Maíllo-Fernández, J.M., Valladas, H., Cabrera, V. & Bernaldo de Quirós, F. (2001) Nuevas dataciones para el Paleolítico Superior de Cueva Morín (Villanueva de Villaescusa, Cantabria). *Espacio, Tiempo y Forma*, 14, 145–150.
Marín-Arroyo, A.B., Rios-Garaizar, J., Straus, L.G., Jones, J.R., de la Rasilla, M., González Morales, M.R. et al. (2018) Correction: Chronological reassessment of the Middle to Upper Paleolithic transition and Early Upper Paleolithic cultures in Cantabrian Spain. *PLoS One*, 13(6), e0199954.
Maroto, J., Vaquero, M., Arrizabalaga, Á., Baena, J., Baquedano, E., Jordá, J. et al. (2012) Current issues in late Middle Palaeolithic chronology: New assessments from Northern Iberia. *Quaternary International*, 247, 15–25.
Martin, L., Mercier, N., Incerti, S., Lefrais, Y., Pecheyran, C., Guérin, G. et al. (2015) Dosimetric study of sediments at the beta dose rate scale: Characterization and modelization with the DosiVox software. *Radiation Measurements*, 81, 134–141.
Martínez-Pillado, V., Aranburu, A., Arsuaga, J., Ruiz-Zapata, B., Gil-García, M., Stoll, H. et al. (2014) Upper Pleistocene and Holocene palaeoenvironmental records in Cueva Mayor karst (Atapuerca, Spain) from different proxies: Speleothem crystal fabrics, palynology, and archaeology. *International Journal of Speleology*, 43, 1–14.
Mejdahl, V. (1979) Thermoluminescence dating: beta-dose attenuation in quartz grains. *Archaeometry*, 21, 61–72.
Mejdahl, V. (1987) Internal radioactivity in quartz and feldspar grains. *Ancient TL*, 5, 10–17.
Montes, L., Utrilla, P. & Hedges, R. (2001) Le passage Paléolithique Moyen-Paléolithique Supérieur dans la Vallée de l'Ebre (Espagne). Datations radiométriques des grottes de Peña Miel et Gabasa. In: Zilhão, J., Aubry, T. & Carvalho, A.F. (Eds.) *Les Premiers Hommes Modernes de La Péninsule Ibérique. Actes Du Colloque de La Commission VIII de l'UISPP*. Lisboa: Instituto Português de Arqueologia. pp. 87–102.
Moreno, D., Ortega, A.I., Falguères, C., Shao, Q., Tombret, O., Gómez-Olivencia, A. et al. (2022) ESR/U-series chronology of the Neanderthal occupation layers at Galería de las Estatuas (Sierra de Atapuerca, Spain). *Quaternary Geochronology*, 72, 101342.
Moreno, J.M., Pineda, F.D. & Rivas-Martinez, S. (1990) Climate and vegetation at the Eurosiberian-Mediterranean boundary in the Iberian Peninsula. *Journal of Vegetation Science*, 1, 233–244.
Moure, A. & García Soto, E. (1982) Datación radiocarbónica del Mousteriense de Cueva Millán (Hortiguela, Burgos). *Boletín del Sedimentario de Estudios de Arte y Arqueología*, 48, 71–72.
Mozota Holgueras, M. (2014) "Less-elaborate" bone tools during the Lower and Middle Paleolithic, and its continuity during the Upper Paleolithic. An historiographical review. *Complutum*, 25, 17–33.
Murray, A., Arnold, L.J., Buylaert, J.P., Guérin, G., Qin, J., Singhvi, A.K. et al. (2021) Optically stimulated luminescence dating using quartz. Nature Reviews Methods Primers 1. 71. https://doi.org/10.1038/s43586-021-00068-5
Murray, A.S. & Wintle, A.G. (2000) Luminescence dating of quartz using an improved single-aliquot regenerative-dose protocol. *Radiation Measurements*, 32, 57–73.
Nathan, R.P., Thomas, P.J., Jain, M., Murray, A.S. & Rhodes, E.J. (2003) Environmental dose rate heterogeneity of beta radiation and its implications for luminescence dating: Monte Carlo modelling and experimental validation. *Radiation Measurements*, 37, 305–313.
Navazo, M., Alonso-Alcalde, R., Benito-Calvo, A., Díez, J.C., Pérez-González, A. & Carbonell, E. (2011) Hundidero: Mis 4 open air neanderthal occupations in sierra de atapuerca. *Archaeology, Ethnology and Anthropology of Eurasia*, 39, 29–41.
Navazo, M., Díez, C., Torres, T., Colina, A. & Ortiz, J.E. (2005) La cueva de Prado Vargas. Un yacimiento del Paleolítico Medio en el sur de la Cordillera Cantábrica. In: Montes, R. & Lasheras, J.A. (Eds.), Actas de La Reunión Científica: Neandertales Cantábricos, estado de la cuestión. Museo Nacional y Centro de Investigación de Altamira, pp. 151-166.
Obermaier, H. (1916) El Hombre Fósil. Comisión de Investigaciones Prehistóricas y Paleontológicas, Madrid.
Olley, J.M., Caitcheon, G.G. & Roberts, R.G. (1999) The origin of dose distributions in fluvial sediments, and the prospect of dating single grains from fluvial deposits using optically stimulated luminescence. *Radiation Measurements*, 30, 207–217.
Olley, J.M., Murray, A. & Roberts, R.G. (1996) The effects of disequilibria in the uranium and thorium decay chains on burial dose rates in fluvial sediments. *Quaternary Science Reviews*, 15, 751–760.
Olley, J.M., Roberts, R.G. & Murray, A.S. (1997) Disequilibria in the uranium decay series in sedimentary deposits at Allen's Cave, Nullarbor Plain, Australia: Implications for dose rate determinations. *Radiation Measurements*, 27, 433–443.
Pawley, S.M., Bailey, R.M., Rose, J., Moorlock, B.S.P., Hamblin, R.J.O., Booth, S.J. et al. (2008) Age limits on Middle Pleistocene glacial sediments from OSL dating, north Norfolk, UK. *Quaternary Science Reviews*, 27, 1363–1377.
Pinto-Llona, A.C., Clark, G., Karkanas, P., Blackwell, B., Skinner, A.R., Andrews, P. et al. (2012) The Sopeña Rockshelter, a New Site in Asturias (Spain) bearing evidence on the Middle and Early Upper Palaeolithic in Northern Iberia. *Munibe*, 63, 45–79.
Pinto-Llona, A.C. & Grandal-d'Anglade, A. (2019) Conflicting 14C scenarios in the Sopeña cave (northern Iberia): Dating the Middle-Upper Palaeolithic boundary by non-ultrafiltered versus ultrafiltered AMS 14C. *Quaternary International*, 522, 1–11.
Prescott, J.R. & Hutton, J.T. (1994) Cosmic ray contributions to dose rates for luminescence and ESR dating: Large depths and long-term time variations. *Radiation Measurements*, 23, 497–500.
Preusser, F. & Degering, D. (2007) Luminescence dating of the Niederweningen mammoth site, Switzerland. *Quaternary International*, 164-165, 106–112.
Quam, R.M., Arsuaga, J.L., Bermúdez De Castro, J., Díez, C.J., Lorenzo, C., Carretero, M. et al. (2001) Human remains from Valdegoba Cave (Huérmeces, Burgos, Spain. *Journal of Human Evolution*, 41, 385–435.
Readhead, M.L. (1987) Thermoluminescence dose rate data and dating equations for the case of disequilibrium in the decay series. *International Journal of Radiation Applications and Instrumentation. Part D. Nuclear Tracks and Radiation Measurements*, 13, 197–207.
Rees-Jones, J. (1995) Optical dating of young sediments using fine-grain quartz. *Ancient TL*, 13, 9–14.
Rees-Jones, J. & Tite, M.S. (1997) Optical Dating Results for British Archaeological Sediments. *Archaeometry*, 39, 177–187.
Reimer, P.J., Austin, W.E.N., Bard, E., Bayliss, A., Blackwell, P.G., Bronk Ramsey, C. et al. (2020) The IntCal20 Northern Hemisphere Radiocarbon Age Calibration Curve (0-55 cal kBP), *Radiocarbon*, 62, 725–757.
Richter, D., Dibble, H., Goldberg, P., McPherron, S.P., Niven, L., Sandgathe, D. et al. (2013a) The late Middle Palaeolithic in Southwest France: New TL dates for the sequence of Pech de l'Azé IV. *Quaternary International*, 294, 160–167.
Richter, D., Hublin, J.J., Jaubert, J., McPherron, S.P., Soressi, M. & Texier, J.P. (2013b) Thermoluminescence dates for the middle palaeolithic site of chez-pinaud Jonzac (France). *Journal of Archaeological Science*, 40, 1176–1185.
Rink, W.J., Schwarcz, H.P., Lee, H.K., Cabrera Valdés, V., Bernaldo De Quirós, F. & Hoyos, M. (1997) ESR dating of Mousterian levels at

El Castillo Cave, Cantabria, Spain. *Journal of Archaeological Science*, 24, 593–600.

Rios-Garaizar, J., Garate Maidagan, D., Gómez-Olivencia, A., Iriarte, E., Arceredillo-Alonso, D., Iriarte-Chiapusso, M.J. et al. (2015) Short-term Neandertal occupations in the late Middle Pleistocene of Arlanpe (Lemoa, northern Iberian Peninsula). *Comptes Rendus Palevol*, 14, 233–244.

Rodríguez de Vera, C., Herrera-Herrera, A.V., Jambrina-Enríquez, M., Sossa-Ríos, S., González-Urquijo, J., Lazuen, T. et al. (2020) Micro-contextual identification of archaeological lipid biomarkers using resin-impregnated sediment slabs. Scientific Reports 10. 10, 20574. https://doi.org/10.1038/s41598-020-77257-X

Ruiz, M.N., Benito-Calvo, A., Alonso-Alcalde, R., Alonso, P., Fuente, H., Santamaría, M. et al. (2021) Late Neanderthal subsistence strategies and cultural traditions in the northern Iberia Peninsula: Insights from Prado Vargas, Burgos, Spain. *Quaternary Science Reviews*, 254, 106795.

Sánchez Goñi, M.F., Landais, A., Fletcher, W.J., Naughton, F., Desprat, S. & Duprat, J. (2008) Contrasting impacts of Dansgaard–Oeschger events over a western European latitudinal transect modulated by orbital parameters. *Quaternary Science Reviews*, 27, 1136–1151.

Sanguino, J. & Montes, R. (2005) Nuevos datos para el conocimiento del Paleolítico Medio en el centro de la Región Cantábrica: la cueva de Covalejos (Pielagos, Cantabria). In: Montes, R. & Lasheras, J.A. (Eds.) *Actas de La Reunión Científica: Neandertales Cantábricos. Estado de La Cuestión*. Madrid: Museo Nacional y Centro de Investigación de Altamira. pp. 489–504.

Santamaría, M., Navazo, M., Benito-Calvo, A., Alonso, R., López, G.I. & Carbonell, E. (2021) Atapuerca Neanderthal landscape at Fuente Mudarra site in Burgos, Spain, during Marine Isotope Stages 5-3. *Quaternary Research*, 99, 248–269.

Slimak, L., Zanolli, C., Higham, T., Frouin, M., Schwenninger, J.L., Arnold, L.J. et al. (2022) Modern human incursion into Neanderthal territories 54,000 years ago at Mandrin, France. *Science Advances* 8, eabj9496. Available from: https://doi.org/10.1126/sciadv.abj9496

Smedley, R.K., Duller, G.A.T., Rufer, D. & Utley, J.E.P. (2020) Empirical assessment of beta dose heterogeneity in sediments: implications for luminescence dating. *Quaternary geochronology*, 56, 101052.

Smith, M.A., Prescott, J.R. & Head, M.J. (1997) Comparison of 14C and luminescence chronologies at Puritjarra rock shelter, central Australia. *Quaternary Science Reviews*, 16, 299–320.

Spindler, L., Comeskey, D., Chabai, V., Uthmeier, T., Buckley, M., Devièse, T. et al. (2021) Dating the last Middle Palaeolithic of the Crimean Peninsula: New hydroxyproline AMS dates from the site of Kabazi II. *Journal of Human Evolution*, 156, 102996.

Stevens, T., Buylaert, J.P. & Murray, A.S. (2009) Towards development of a broadly-applicable SAR TT-OSL dating protocol for quartz. *Radiation Measurements*, 44, 639–645.

Talamo, S., Aldeias, V., Goldberg, P., Chiotti, L., Dibble, H.L., Guérin, G. et al. (2020) The new ^{14}C chronology for the Palaeolithic site of La Ferrassie, France: the disappearance of Neanderthals and the arrival of Homo sapiens in France. *Journal of Quaternary Science*, 35, 961–973.

Utrilla, P., Mazo, C. & Domingo, R. (2015) Fifty thousand years of prehistory at the cave of Abauntz (Arraitz, Navarre): A nexus point between the Ebro Valley, Aquitaine and the Cantabrian Corridor. *Quaternary International*, 364, 294–305.

Vernot, B., Zavala, E.I., Gómez-Olivencia, A., Jacobs, Z., Slon, V., Mafessoni, F. et al. (2021) Unearthing Neanderthal population history using nuclear and mitochondrial DNA from cave sediments. *Science*, 372(Issue 6542). eabf1667 Available from: https://doi.org/10.1126/science.abf1667

Wood, R., Bernaldo de Quirós, F., Maíllo-Fernández, J.M., Tejero, J.M., Neira, A. & Higham, T. (2018) El Castillo (Cantabria, northern Iberia) and the Transitional Aurignacian: Using radiocarbon dating to assess site taphonomy. *Quaternary International*, 474, 56–70.

Wood, R.E., Barroso-Ruíz, C., Caparrós, M., Jordá Pardo, J.F., Santos, B.G. & Higham, T.F.G. (2013b) Radiocarbon dating casts doubt on the late chronology of the Middle to Upper Palaeolithic transition in southern Iberia. *Proceedings of the National Academy of Sciences of the United States of America*, 110, 2781–2786.

Wood, R.E., Higham, T.F.G., De Torres, T., Tisnérat-Laborde, N., Valladas, H., Ortiz, J.E. et al. (2013a) A new date for the neanderthals from el sidrón cave (asturias, northern spain). *Archaeometry*, 55, 148–158.

Zilhão, J. (2021) The late persistence of the Middle Palaeolithic and Neandertals in Iberia: A review of the evidence for and against the "Ebro Frontier" model. *Quaternary Science Reviews*, 270, 107098.

Zilhão, J., Angelucci, D.E., Arnold, L.J., Demuro, M., Hoffmann, D.L. & Pike, A.W.G. (2021a) A revised, Last Interglacial chronology for the Middle Palaeolithic sequence of Gruta da Oliveira (Almonda karst system, Torres Novas, Portugal). *Quaternary Science Reviews*, 258, 106885. Available from: https://doi.org/10.1016/j.quascirev.2021.106885

Zilhão, J., Angelucci, D.E., Arnold, L.J., d'Errico, F., Dayet, L., Demuro, M. et al. (2021b) Revisiting the Middle-to-Upper Palaeolithic transition at Gruta do Caldeirão (Tomar, Portugal). *PLoS One*, 16(10), e0259089. Available from: https://doi.org/10.1371/journal.pone.0259089

Zilhão, J., Angelucci, D.E., Igreja, M.A., Arnold, L.J., Badal, E., Callapez, P. et al. (2020) Last Interglacial Iberian Neandertals as fisher-hunter-gatherers. *Science*, 367, 6485.